SANDIA REPORT
SAND2010-6704
Unlimited Release
Printed September 2010

Final LDRD report: Efficient Multi-exciton emission from quantum dots

Ting S. Luk

Prepared by Sandia National Laboratories Albuquerque, New Mexico 87185 and Livermore, California 94550

Sandia National Laboratories is a multi-program laboratory managed and operated by Sandia Corporation, a wholly owned subsidiary of Lockheed Martin Corporation, for the U.S. Department of Energy's National Nuclear Security Administration under contract DE-AC04-94AL85000
Approved for public release; further dissemination unlimited.

Sandia National Laboratories

Issued by Sandia National Laboratories, operated for the United States Department of Energy by Sandia Corporation.

NOTICE: This report was prepared as an account of work sponsored by an agency of the United States Government. Neither the United States Government, nor any agency thereof, nor any of their employees, nor any of their contractors, subcontractors, or their employees, make any warranty, express or implied, or assume any legal liability or responsibility for the accuracy, completeness, or usefulness of any information, apparatus, product, or process disclosed, or represent that its use would not infringe privately owned rights. Reference herein to any specific commercial product, process, or service by trade name, trademark, manufacturer, or otherwise, does not necessarily constitute or imply its endorsement, recommendation, or favoring by the United States Government, any agency thereof, or any of their contractors or subcontractors. The views and opinions expressed herein do not necessarily state or reflect those of the United States Government, any agency thereof, or any of their contractors.

Printed in the United States of America. This report has been reproduced directly from the best available copy.

Available to DOE and DOE contractors from
U.S. Department of Energy
Office of Scientific and Technical Information
P.O. Box 62
Oak Ridge, TN 37831

Telephone: (865) 576-8401
Facsimile: (865) 576-5728
E-Mail: reports@adonis.osti.gov
Online ordering: http://www.osti.gov/bridge

Available to the public from
U.S. Department of Commerce
National Technical Information Service
5285 Port Royal Rd.
Springfield, VA 22161

Telephone: (800) 553-6847
Facsimile: (703) 605-6900
E-Mail: orders@ntis.fedworld.gov
Online order: http://www.ntis.gov/help/ordermethods.asp?loc=7-4-0#online

SAND2010-6704
Unlimited Release
Printed September 2010

Efficient Mult-exciton emission from quantum dots

Ting S. Luk
Org 1725
Sandia National Laboratories
P.O. Box 5800
Albuquerque, New Mexico 87185-MS1080

Abstract

The fundamental spontaneous emission rate an emitter can be modified by its photonic environment. By enhancing the spontaneous emission rate, there is a possibility of extracting multi-exciton energies through radiative decay. In this report, we explore using high Q and small volume cavities to enhance the spontaneous emission rate. We observed greater than 50 folds enhancement in the spontaneous emission from photonic crystal waveguide or microcavity using close-packed monolayer of PbS quantum dot emitters.

ACKNOWLEDGMENTS

The successful completion of this project is the result of the efforts of many people: Ihab El-Kady, Mehmet Su, and Bernardo Farfan for performing FDTD numerical simulations; Jeff Brinker and Shisheng Xiong for developing integration techniques to transfer or embed QDs into 2D and 3D photonic crystal; Paul Resnick for fabricating 2D and 3D photonic crystal; Weng Chow for scientific guidance and simulating discussions; Ganesh Subramania, Mike Sinclair, Rohan Ketatpure, Xiaoyu Miao, Alon Gabbay and Art Fischer for discussions and helping in experimental data interpretation in this project.

Table of content

Acknowledgments		4
1.	Introduction	6
2.	Integrating colloidal quantum dots with photonic crystals	7
3.	Enhanced emission of PbS quantum dots in 2D photonic crystal microcavity	12
4.	Ultra-small volume plasmonic nanocavity for enhancing quantum dot emission	28
5.	Conclusions	39
Distribution		40

1. Introduction

Multi-exciton generation can have an important impact to the solar energy harvesting. While the efficiency of this process in quantum dots system is far less than originally thought, detail understanding of the underlying physical mechanisms is important to many applications using quantum dots. This project is motivated by the possibility of converting the multi-exciton energies into radiative emissions thus realizing a novel optical down conversion similar to a step down transformer for voltage control. Ability to optically down convert energy photon energy into lower photon energy can also enable solar energy harvesting of energetic photons.

The approach taken in this project is to enhance the spontaneous emission rate to a level sufficiently high so that radiative decay rate becomes the dominant relaxation channel. This requires large radiative enhancement factor. Large radiative enhancement factor can be realized in low loss (high Q-factor) and small volume cavities, commonly known as Purcell effect. However, if the Q-factor of the cavity is too high compare to the emitter's homogeneous linewidth, the benefit of the high Q cavity diminish. This approach puts a severe limitation on its ability to realize very large radiative enhancement effect as we find out in the course of this project. The type of photonic cavity used in this approach is microcavity in 2D Si photonic crystal. Since the goal is to enhance emission of colloidal quantum dots, the first problem the project need to address is how to integrate quantum dots with the photonic crystal without severely degrading the Q factor of the cavity and has the uniformity and reliability so that systematic measurements can be made on the system. Section 2 describes the method of integration chosen and the results of optical characterization, interpretation and analysis are in section 3.

An alternate approach is to use very small volume cavity. In order to create a cavity much smaller than the emission wavelength, a metallic structure is required. We have explored the enhancement effect of an emitter placed inside a metallic cavity. In this approach, although the maximum quantum efficiency can only reach 50%, it is a very effective approach for bad emitters (see section 4). In addition, this approach can protect the quantum dot emitter from the environment which enables integrating the emitter in various chemical and biological systems.

2. Integrating colloidal quantum dots with photonic crystals

In a microcavity, the emission rate is maximum if a quantum dot is located at the antinode of the cavity. Instead of selectively placing one or a cluster of quantum dot on a specific location of the cavity such as using an AFM tip, we chose to blanket the photonic crystal with a continuous film of quantum dots. If the quantum density is high enough, the problem of matching the quantum dot location to the antinode is circumvented. There remains a problem of controlling the location of the quantum dot in the out-of-plane direction. The method described below using evaporative self-assembly technique takes advantage of the hydrophobic force of the capping molecules on quantum dots in a polymer film so that the quantum dots are preferentially resides at the air-polymer interface. This film is subsequently transferred to the photonic crystal to enable quantum dots to have an intimate contact to the photonic crystal. The following is a reprint of the manuscript published in Small.

small

Photonic crystals

Integration of a Close-Packed Quantum Dot Monolayer with a Photonic-Crystal Cavity Via Interfacial Self-Assembly and Transfer

Shisheng Xiong, Xiaoyu Miao, Jeffrey Spencer, Constantine Khripin, Ting S. Luk, and C. Jeffrey Brinker**

Nanoparticle (NP) assembly into ordered 2- and 3-D superlattices has stimulated enormous recent interest as a means to create new artificial solids whose electronic, magnetic, and optical behaviors can be tailored by the size dependent properties of the individual NPs mediated by coupling interactions with neighboring NPs,[1,2] suggesting applications in a diverse range of technologies including photovoltaics,[3] sensors,[4] catalysis,[5] and magnetic storage.[6] To date superlattice assembly has been demonstrated for monosized,[7] binary,[8] and even ternary systems,[9] allowing development and interrogation of a range of collective behaviors: electron transport within 2- and 3-D arrays of Coulomb islands,[10,11] Forster resonance energy transfer between superlattice monolayers in close proximity,[12] switchable optical properties through regulation of NP d-spacing,[1] and new magnetic behaviors based on binary superlattices.[13] Superlattice fabrication is performed principally by droplet evaporation[14] or convective assembly on an inclined plate.[15,16] These techniques are often slow, restricted in the size and topography of the substrate, and result in van der Waals solids with limited mechanical behaviors. To address these issues, we recently reported a general, rapid method to prepare large area, free-standing, NP/polymer monolayer superlattices by interfacial NP assembly within a polymer film on a water surface.[17] Although it is well known that the Langmuir-Blodgett technique has been used to produce well-controlled nanoparticle films,[18,19] our ultra-thin superlattices are highly robust and transferable to arbitrary substrates, owing to the polymer supporting layer.

Here we demonstrate interfacial self-assembly and transfer as an approach to address a long-standing technology challenge: how to integrate colloidal light emitters (e.g. semiconductor quantum dots) with a nanophotonic structure in a manner that achieves good quantum dot (QD) coupling with anti-nodes of the optical microcavity and avoids significant Q factor degradation. Enhancement of spontaneous emission from photo emitters coupled to the photonic crystal microcavity based on the Purcell effect[20] provides an ideal test for the integration of bottom-up self-assembly with top-down nanofabrication and means to study emitter behavior in microcavities. Standard spin-coating cannot achieve a high QD density, uniform film thickness, or controlled uniform separation between QDs over the photonic crystal surface.[21] Fabrication of a photonic crystal cavity around a single pre-screened Stranski-Krastanow grown QD with the desired optical properties is laborious, although exquisite control in position and wavelength is possible.[22] Templated growth of single quantum dots on GaAs (111)B surfaces has been demonstrated to provide good spatial control,[23] but suffers from low QD density and the requirement for precise control of the emission wavelength for high Q cavity applications.

Interfacial self-assembly (**Figure 1**a) provides a facile, rapid, scalable approach to assemble and transfer a large area NP array uniformly to a topographically complex photonic crystal surface (**Figure 2**). The transferred ultra-thin close-packed QD monolayer provides high density, uniformity and robustness, and controllable film thickness.[17] A seamless conformal interface between the QD monolayer and the photonic crystal microcavity is realized by either a 'picking' or 'lifting' transfer procedure (see Figure 1b and c). This allows optimal coupling between QDs and the photonic-crystal cavity, while relaxing the requirement of positioning individual QDs. Tuning the cavity resonance to the dot emission becomes unnecessary because the QD has a broad emission bandwidth. The uniformity and close proximity of the NP monolayer to the photonic crystal (Figure 2b, c) surface allows us to demonstrate an enhanced spontaneous emission of infrared quantum dots coupled to the defect cavity, while maintaining high Q.

S. Xiong, C. Khripin, Prof. C. J. Brinker
Department of Chemical and Nuclear Engineering
University of New Mexico
Albuquerque, NM 87106, USA
E-mail: cjbrink@sandia.gov

X. Miao, Dr. T. S. Luk, Prof. C. J. Brinker
Sandia National Laboratories
P.O. Box 5800, Albuquerque, NM 87185, USA
E-mail: tsluk@sandia.gov

X. Miao, Dr. T. S. Luk
Center for Integrated Nanotechnologies
Sandia National Laboratories
P.O. Box 5800, Albuquerque, NM 87185, USA

J. Spencer
Department of Mechanical Engineering
University of New Mexico
Albuquerque, NM 87106, USA

DOI: 10.1002/smll.201000897

© 2010 Wiley-VCH Verlag GmbH & Co. KGaA, Weinheim

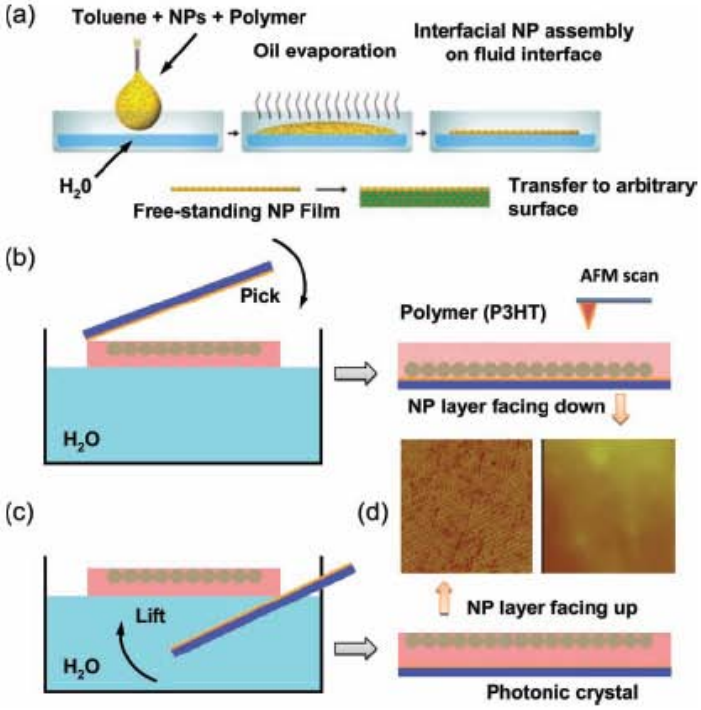

Figure 1. a) Schematic of the evaporation induced interfacial assembly and transfer process. b) Film transfer to the photonic crystal cavity by picking process results in a monolayer where the QDs are in close contact with the photonic crystal surface. c) For lifting, the QDs are about 20–50-nm away from the photonic crystal in the vertical direction. The AFM images (d) show the surface topography for the original vapor-side interface (AFM image of lifted monolayer) and for the original water-side interface. The dimension of the scanned image is 250 × 250 nm.

Self-assembly of the close-packed PbS QD/polymer monolayer was based on the interfacial evaporation induced self-assembly (EISA) procedure we recently reported,[17] and which we summarize briefly here. Oleic acid ligated PbS QDs (purchased from Evident Technologies) were dissolved in toluene containing polythiophene (P3HT) (interfacial assembly can be performed with many different polymers; P3HT is a representative example). One drop (about 8 µl) of the QD/P3HT/toluene solution was dispensed quickly by a syringe onto the surface of deionized water contained in a Petri dish. The droplet immediately spread into a film of ca. 5 cm diameter on the water surface. Solvent evaporation drives QD self-assembly followed by solidification within P3HT, the water interface maintaining the required QD mobility needed to achieve a highly ordered low defect QD monolayer. The resulting monolayer film is only 20 – 50 nm thick as determined by ellipsometry. The film thickness can be controlled by the polymer concentration in the solution (0.5–5 mg/ml in the case of P3HT). The hydrophobic PbS QDs reside preferentially at the air/polymer interface as determined by X-ray reflectivity measurements[24] and atomic force microscopy (AFM, see below). To transfer the monolayer to a photonic crystal or other device, we use the 'picking' or 'lifting' transfer procedures, respectively. As shown in Figure 1b, the picking process consists of lowering the photonic crystal device (see supporting information for fabrication process of the photonic crystal device; SEM images shown in Figure 2a, b.) from the air side toward the floating monolayer with the functional surface of the photonic crystal face down as illustrated in Figure 1b. This enables the QDs to be in close contact with the photonic crystal cavity, since the QDs reside at the polymer/air interface of the interfacially assembled array. In this case, the QDs and the photonic crystal are separated by only the stabilizing oleic acid ligand. To remove any residual water that might have been trapped in the film, the device was annealed at 100 °C for 5 minutes in air. For plasmonic applications where it is desirable to have a dielectric spacer between the QDs and the device surface in order to reduce the non-radiative damping,[25] the 'lifting' technique is more suitable. In this case, the photonic crystal substrate is first lowered into the water without touching the floating film, and then the substrate is retracted capturing the floating film with the polymer side down (Figure 1c).). The proximity of the QDs to the original vapor or water interfaces of the interfacially assembled monolayer is evident from AFM images of films transferred to silicon substrates by lifting or picking (Figure 1d). We observe an ordered nanoparticle surface topography for the original vapor side interface (AFM image of lifted monolayer) and a featureless topography for the original water interface (AFM image of picked monolayer). Here AFM is of course probing the opposite side of the film topography in contact with the photonic crystal surface for both transfer procedures.

We have obtained high quality PbS monolayer arrays using both P3HT and polystyrene polymers. It is important to note that, in both procedures the QD monolayer film remains freely suspended over the photonic-crystal surface without deforming and adhering to the side walls of the cavity. For example, Figure 2d shows a free-standing film suspended over a corner feature of the device. This is because the transferred QD/polymer film formed by this evaporation-induced interfacial assembly method is adherent and has a high elastic modulus. To directly measure the mechanical properties of the nanoparticle/polymer composite film, the monolayer array was transferred to a copper substrate with a single 150 µm diameter circular hole in the center via the lifting process. The deflections of the film under different AFM nano-indentation forces are shown in Figure S2. The Young's modulus of the PbS-P3HT film was determined to be about $10^{[9]}$ Pa using a simplified Reissner analysis.[26] To confirm that the quantum dots are indeed in a close-packed configuration, the film can be transferred to a TEM grid and examined as shown in Figure 2c. The density of

© 2010 Wiley-VCH Verlag GmbH & Co. KGaA, Weinheim

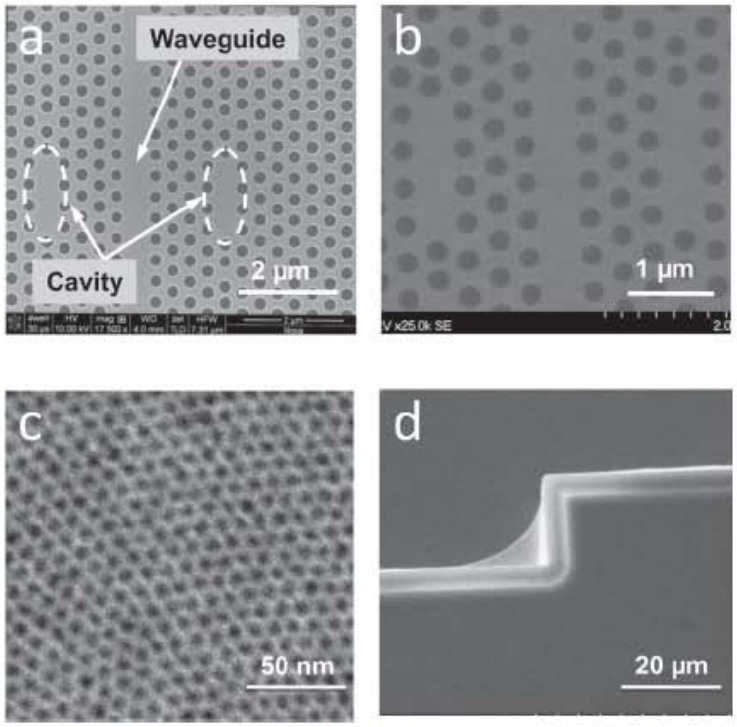

Figure 2. a,b) SEM images of a photonic crystal device before (a) and after (b) coating with a PbS-P3HT composite monolayer film. c) TEM image of the PbS-P3HT monolayer. d) a SEM image of a freely suspended monolayer spanning a corner feature of the device (This freely suspended region is used as a control to monitor optical properties of the monolayer itself).

the PbS QD in our sample is estimated from the TEM image to be about 2×10^{12} cm^{-2} with film non-uniformity less than 20%. As determined by GISAXS[24] interfacial assembly and transfer procedure allows us to achieve an ordered (uniform) close-packed QD array over large areas.

To demonstrate the importance of having the QD array in close contact with the photonic crystal cavity, we compared the enhanced photoluminescence (see supporting information for details of the optical characterization setup) from samples prepared by the 'picking' and 'lifting' transfer processes. **Figure 3**a shows a dramatic enhancement in photoluminescence from the cavity mode for the QD film transferred to the photonic crystal by picking (blue curve) versus the supported QD film transferred by lifting (red curve). The difference between the two photoluminescence measurements is consistent with the fact that the 'picking' process allows the QDs to be in close contact with the photonic-crystal cavity, providing better coupling to the cavity and thereby yielding a larger enhancement. In contrast, for the 'lifting' process, the coupling is dramatically reduced despite the QDs being separated by only 20–50 nm from the cavity in the vertical direction. In both samples, resonances are observed at about 1460 nm with the electric field polarized parallel to the waveguide axis. The broad background from the photoluminescence of QDs is similar to that obtained from a free-standing QD-polymer film (Figure 2d). The enhancement factor from the 'picking' process is about 7 times larger than the 'lifting' process. This ratio is consistent with a typical field decay length of 50 nm[27] and a typical film thickness of 50 nm. The emission lifetime of the 'picking' sample should be shorter than the 'lifting' sample. In these experiments, we made no attempt to use more mono-dispersed quantum dots than those commercially available. We estimate on average there are 20 QDs per nm bandwidth residing on the antinodes of the microcavity. With such a small number of emitters in a monolayer film, radiative lifetime measurement is proved to be difficult because of low emission rate (1–3 μsec radiative lifetime) and lack of suffciently low noise photon counting detector in this wavelength region. The highest Q factor observed with this deposition technique is about 8060 as shown in Figure 3(b), where the polarization of the photoluminescence is perpendicular to the waveguide axis To the best of our knowledge, this is the highest Q factor ever achieved using colloidal QDs coupled to a photonic crystal microcavity. We believe this Q factor reflects the quality of the photonic crystal rather than the transferred film. Numerical simulations have shown that theoretically the cavity Q with this polymer film can be as high as 25,000.[28]

In order to ensure the enhanced emission is not due to amplified spontaneous emission, we also measured the power dependence of the resonance position and Q factor of the photonic crystal cavity (data not shown here). We use the the Q factor and the ratio between the peak and the off resonant background near the resonance as indicators of amplified spontaneous emission effect. Within the resolution of the measurements (0.15 nm), we have not observed increase in Q factor nor any significant change in the peak to background ratio; constant to within 20% over several orders of magnitude change in the laser power. The intensity dependent data (not shown here) of composite films using P3HT and polystyrene are virtually identical, indicating that there is no change in the emission behavior that might have caused by charge transfer in P3HT; this result is consistent with Noone et. al.[29] In addition, the resonance location is independent of excitation intensity which implies the heating from the excitation laser has no impact to our studies.

In summary, we present a new and robust approach to deposit a uniform, densely packed and highly ordered QD/polymer monolayer onto a high Q photonic crystal cavity. A Q factor higher than 8000 has been achieved, indicating the compatibility of this technique with high Q cavities. This approach will enable applications that require integration of active nano-photonic emitting materials with passive micro-photonic structures.

© 2010 Wiley-VCH Verlag GmbH & Co. KGaA, Weinheim

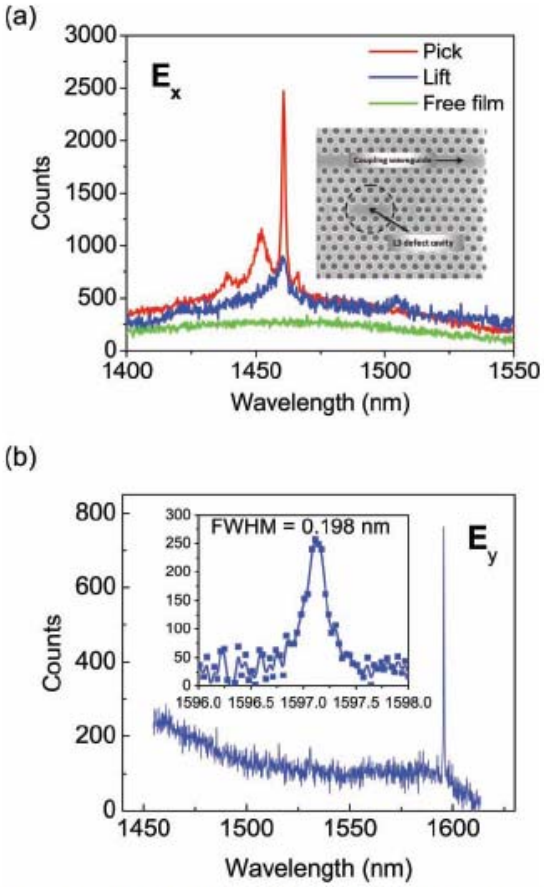

Figure 3. a) Comparison of PL signals from the QD-photonic crystal cavity systems prepared by picking or lifting transfer processes. The inset denotes the region of excitation marked by a black dashed circle. This resonance is referred to as E_x resonance with its emission polarization parallel to the waveguide. Also shown is the PL from a free-standing monolayer PbS-P3HT film. The PL is collected by a spectrometer with a 300 g/mm grating and 50 µm slit width. b) Enhanced photoluminescence spectrum of E_y resonance of an L3 photonic crystal microcavity collected by a spectrometer with a 300 g/mm grating and 50 µm slit width. The polymer used in the sample for this experiment is polystyrene. The inset shows a high-resolution measurement of the same resonance measured with a 900 g/mm grating and a 10 µm slit width. This resonance inherently has a much higher Q factor. The linewidth of the resonance is measured to be 0.198 nm and the corresponding Q factor is 8060.

Acknowledgements

This work is funded by the LDRD program of the Sandia National Laboratories and U.S. Department of Energy Office of Basic Energy Sciences NSET grant DE-FG02–02-ER15368 and the Office of Basic Energy Sciences Division of Materials Sciences and Engineering. Part of the work is performed at the Center for Integrated Nanotechnologies, a U.S. Department of Energy, Office of Basic Energy Sciences user facility. Sandia National Laboratories is a multi-program laboratory operated by Sandia Corporation, a Lockheed-Martin Company, for the U.S. Department of Energy under Contract No. DE-AC04–94AL85000.

[1] C. P. Collier, R. J. Saykally, J. J. Shiang, S. E. Henrichs, J. R. Heath, *Science* **1997**, *277*, 1978–1981.
[2] M. P. Pileni, *Abstracts of Papers of the American Chemical Society* **2001**, *222*, U218–U218.
[3] B. Oregan, M. Gratzel, *Nature* **1991**, *353*, 737–740.
[4] C. Y. Jiang, S. Markutsya, Y. Pikus, V. V. Tsukruk, *Nature Materials* **2004**, *3*, 721–728.
[5] M. Haruta, *Gold Bulletin* **2004**, *37*, 27–36.
[6] S. H. Sun, C. B. Murray, D. Weller, L. Folks, A. Moser, *Science* **2000**, *287*, 1989–1992.
[7] T. P. Bigioni, X. M. Lin, T. T. Nguyen, E. I. Corwin, T. A. Witten, H. M. Jaeger, *Nature Materials* **2006**, *5*, 265–270.
[8] E. V. Shevchenko, D. V. Talapin, N. A. Kotov, S. O'Brien, C. B. Murray, *Nature* **2006**, *439*, 55–59.
[9] W. H. Evers, H. Friedrich, L. Filion, M. Dijkstra, D. Vanmaekelbergh, *Angewandte Chemie-International Edition* **2009**, *48*, 9655–9657.
[10] T. B. Tran, I. S. Beloborodov, J. S. Hu, X. M. Lin, T. F. Rosenbaum, H. M. Jaeger, *Physical Review B* **2008**, *78*.
[11] H. Y. Fan, K. Yang, D. M. Boye, T. Sigmon, K. J. Malloy, H. F. Xu, G. P. Lopez, C. J. Brinker, *Science* **2004**, *304*, 567–571.
[12] M. Achermann, M. A. Petruska, S. A. Crooker, V. I. Klimov, *Journal of Physical Chemistry B* **2003**, *107*, 13782–13787.
[13] E. V. Shevchenko, D. V. Talapin, C. B. Murray, S. O'Brien, *Journal of the American Chemical Society* **2006**, *128*, 3620–3637.
[14] X. M. Lin, H. M. Jaeger, C. M. Sorensen, K. J. Klabunde, *Journal of Physical Chemistry B* **2001**, *105*, 3353–3357.
[15] D. V. Talapin, E. V. Shevchenko, M. I. Bodnarchuk, X. C. Ye, J. Chen, C. B. Murray, *Nature* **2009**, *461*, 964–967.
[16] D. K. Smith, B. Goodfellow, D. M. Smilgies, B. A. Korgel, *Journal of the American Chemical Society* **2009**, *131*, 3281–3290.
[17] J. B. Pang, S. S. Xiong, F. Jaeckel, Z. C. Sun, D. Dunphy, C. J. Brinker, *Journal of the American Chemical Society* **2008**, *130*, 3284-+.
[18] V. Santhanam, J. Liu, R. Agarwal, R. P. Andres, *Langmuir* **2003**, *19*, 7881–7887.
[19] A. P. Kulkarni, K. M. Noone, K. Munechika, S. R. Guyer, D. S. Ginger, *Nano Letters* **2010**, *10*, 1501–1505.
[20] E. M. Purcell, *Physical Review* **1946**, *69*.
[21] I. Fushman, D. Englund, J. Vuckovic, *Applied Physics Letters* **2005**, *87*.
[22] K. Hennessy, A. Badolato, M. Winger, D. Gerace, M. Atature, S. Gulde, S. Falt, E. L. Hu, A. Imamoglu, *Nature* **2007**, *445*, 896–899.
[23] A. Surrente, P. Gallo, M. Felici, B. Dwir, A. Rudra, E. Kapon, *Nanotechnology* **2009**, *20*, 415205.
[24] Shisheng Xiong, Darren Dunphy, Zhang Jiang, Jing Wang, C. J. Brinker, to be published.
[25] J. R. Lakowicz, K. Ray, M. Chowdhury, M. Szymanska, J. Zhang, K. Nowaczyk, *Analyst* **2008**, *133*.
[26] U. Komaragiri, M. R. Begley, J. G. Simmonds, *Trans. ASME, J. Appl. Mech.* **2005**, *72*, 203–212.
[27] J. T. Robinson, S. F. Preble, M. Lipson, *Optics Express* **2006**, *14*, 10588–10595.
[28] T. S. Luk, W. W. Chow, S. Xiong, X. Miao, B. G. Farfan, I. El-Kady, P. J. Resnick, M. F. Su, G. Subramania, M. R. Taha, C. J. Brinker, to be published.
[29] K. M. Noone, N. C. Anderson, N. E. Horwitz, A. M. Munro, A. P. Kulkarni, D. S. Ginger, *Acs Nano* **2009**, *3*, 1345–1352.
[30] Y. Akahane, T. Asano, B. S. Song, S. Noda, *Nature* **2003**, *425*.

Received: May 25, 2010
Revised: July 21, 2010
Published online:

© 2010 Wiley-VCH Verlag GmbH & Co. KGaA, Weinheim

3. Enhanced emission of PbS quantum dots in 2D photonic crystal microcavity

For small low loss photonic cavity designs, photonic crystal microcavities can achieve mode volume as small as 0.15 $(\lambda/n)^3$, where λ is the resonant wavelength and n is the index of refraction of the cavity material. In this project, we use a cavity with a mode volume of 0.95 $(\lambda/n)^3$ in a Si photonic crystal with triangular lattice. In this study, we observed more than 50 fold enhancement in the emission.

Study of Enhanced Emission PbS Quantum Dots on a Photonic-Crystal Microcavity

T-S. Luk[1,2]*, S. Xiong[3], W. W. Chow[2,4], X. Miao[5], M. F. Su[6], P. J. Resnick[2], G. Subramania[2], A.J. Fischer[2], C. J. Brinker[2,3]

[1]*Center for Integrated NanoTechnologies, Sandia National Laboratories, Albuquerque, NM 87123, USA*

[2] *Sandia National Laboratories, Albuquerque, New Mexico 87185-1086, USA*

[3] *Center for MicroEngineered Materials, Department of Chemical and Nuclear Engineering, University of New Mexico, Albuquerque, NM 87106, USA*

[4] *Physics Department and Institute of Quantum Studies, Texas A&M University, College Station, Texas 77843, USA*

[5] *Google Inc, 1600 Amphitheatre Pkwy, Mountain View, CA 94043,*

[6] *Department of Electrical Engineering, University of New Mexico, Albuquerque, NM 87106, USA*

*tsluk@sandia.gov

Abstract: We report a significant enhancement from lithographically-produced photonic crystals with post-processing quantum dot (QD) incorporation. Our analysis shows that the observed enhancement cannot be explained by the combined effects of Purcell enhancement and dielectric enhancement with microscopic local field. We speculate that close-packed superlattice quantum dot structure may have a role in transferring energy into the cavity.

©2009 Optical Society of America

OCIS codes: (230.0230) Photonic crystals; (140.3945) Microcavities; (350.4238) Nanophotonics and photonic crystals; (300.2140) Emission.

References and links

1. Introduction

Quantum-dot emission in a microcavity has been intensively investigated recently due to rapid advances in achieving simultaneously high Q and small volume cavities [1]. Semiconductor quantum dot emitters in microcavities have the potential to realize practical devices such as zero threshold lasers[2], single and entangled photon sources[3][4], as well as quantum optics research[5-8]. In addition, the ability to enhance the emission rate by virtue of Purcell effect [9]is also important to silicon photonics[10], solid state lighting [11-12]and solar cell applications [12-13].

In the case of good emitters such as InAs quantum dots, in which the total dephasing and the radiative linewidth are both much smaller than the cavity linewidth, large enhancement in spontaneous emission have been clearly demonstrated in the weak coupling regime[9, 14-15]. Recently, strong coupling behavior has also been demonstrated [16-18]. Current understanding of non-ideal or "bad emitter" systems in which the dephasing width is much larger than the radiative width and the cavity linewidth, is less clear[19-25]. Examples of bad emitters are PbS and PbSe colloidal quantum dots, Si nanocrystals and Er^{3+} ions in SiO_2 or silicon nitride. According to several theoretical studies[26-28], for emitter systems like PbS and PbSe quantum dots, the Purcell enhancement is negligible and is independent of the cavity Q factor but rather is determined by the emitter Q factor. Experimentally reported enhancement factors from "bad emitters" have large amount of variation. A Purcell enhancement factor of 30 was reported by spin coating colloidal PbS quantum dots embedded in polymethylmethacrylate (PMMA) on photonic crystal microcavity of Q=400. An enhancement

factor of 10 has also been reported with a cavity Q of 3000[23] using selective chemical attachement activated by AFM nanopatterning. In another case, PbS quantum dots were attached to the cavity by soaking which yielded an enhancement factor of 35 from a cavity with Q=775[21]. And for Er^{3+}ion in silicon nitride, a room temperature enhancement factor of 1.4 was reported from a cavity with Q=6000[29]. None of these studies have demonstrated enhancement factor that varies with Q factor. For a PbS studies, the reported enhancement factor is significantly larger than what is expected based on the observed linewidth of 26meV from low temperature photoluminescence studies [30]. A even broader homogeneous linewidth of 100meV has been determined from smaller PbS quantum dots [31-32] emitting at 800nm. In addition, the impact of spectral diffusion effect is not known. In all these studies except for the AFM patterning case, the emitter locations with respect to the surface of the photonic crystal are not well defined. There are also other unknowns such as the exact property of the quantum dots that are responsible for the enhanced emission and its interaction with the material of the microcavity.

In this study, we attempt to eliminate one of these unknowns by placing a 20-50nm thick polymer film with a monolayer of close-packed PbS onto the surface of a photonic crystal microcavity where these quantum dots are located only at the interface between the polymer and the photonic crystal. In this case, the surface of the cavity is uniformly covered with quantum dots and therefore there are an equal number of dots on the node and antinode region of the cavity [33]. This removes one of the unknowns in the emission behavior. The highest Q factor achieved with this technique is greater than 8000. After studying a large number of cavity-emitter structures, no clear linear relationship between the enhancement factor and the cavity Q has been found which suggests that our measurements are consistent with the “bad emitter” regime. However, the enhancement factor observed is larger than the dielectric enhancement effect can produce, which suggests that there are other enhancement mechanisms at play.

2. Fabrication of photonic crystal and close-packed monolayer polymer film

For photonic crystal and microcavity fabrication, the starting material is 150 mm diameter silicon-on-insulator (SOI) wafer with 250nm thick silicon device layer with 3μm thick buried-oxide (BOx) layer. The pattern is a triangular lattice with lattice constant in the Γ-K direction of a=415nm and holes diameter of 240nm. A cavity is created in the photonic crystal lattice by three missing air holes (L3) shown in Fig. 1a-c. The cavity has the end-hole positions shifted away from the cavity by a nominal value of 0.18a, 0.025a, and 0.18a, as in the design by Akahane et. al.[34]. Devices fabricated have 100-300 holes in the Γ-K direction with a waveguide along this direction and 15 holes in the Γ-X direction. We use commercially available, mass-production semiconductor processing tools throughout the fabrication process. A waveguide is also fabricated which can be used to couple an external source into the microcavity. The coupling strength is controlled by the number of holes between the waveguide and the cavity. In particular, we will discuss result associated with the $1.1W_1$ waveguide which has a width 10% larger than it would have been with a row of missing holes.

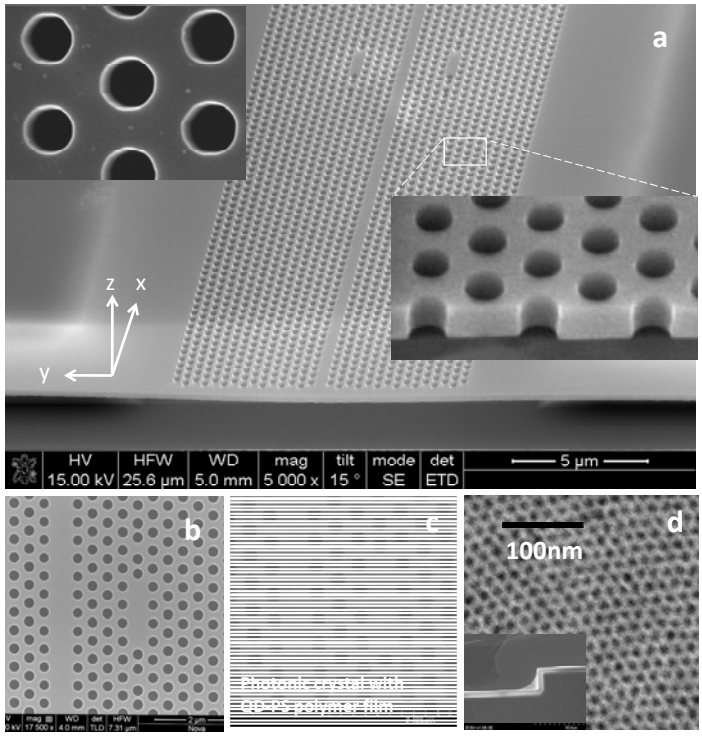

Fig. 1. (a) SEM image of a 2D silicon membrane photonic crystal device consists of two L3 cavities and a waveguide supported with SiO_2 anchors. The top left inset shows the top view of the holes on the silicon membrane. The lower right inset shows the side wall profile of the holes. (b) Top SEM view of the L3 cavity created by three missing air holes. (c) SEM image of a cavity with polymer film on top. (d) TEM image of a monolayer of PbS in P3HT polymer. Lower left inset shows a free-standing film hanged by a corner feature of the photonic crystal sample.

All lithography was performed on an ASML PAS 5500 Step-and-Scan system, and all dry etching was performed with Applied Materials Centura platform tools. The first lithographic layer defines the photonic crystal by patterning 240nm holes in the photoresist. This pattern is transferred into the device layer using reactive ion etching (RIE), optimized for vertical sidewalls. A second mask level was used to etch the substrate on either side of the device for optical access. A deep reactive ion etch (DRIE) was used to create roughly 80µm deep grooves into the silicon to provide optical coupling of the lens fiber to the waveguides. To protect the photonic crystal that had been etched into the device layer, an 8.5 kÅ polysilicon film was deposited on top of a 2µm thick oxide film and then patterned with a photoresist mask. The polysilicon hard mask was used for the oxide etch steps because relatively thick oxide films were employed (2µm hard mask, 3µm BOx). The oxide film served as a hard mask for the DRIE Si etch. During the BOx etch, the photoresist mask is consumed and the polysilicon hard mask is used to define the pattern. During the DRIE handle etch, the polysilicon mask is also consumed so that the underlying 2µm oxide film now acts as the mask to protect the silicon photonic crystal device. Finally, hydrofluoric acid (HF) was used to strip the remaining oxide hard mask, as well as to undercut the SOI buried oxide below the

lattice. A timed etch was used such that the oxide was stripped below the lattice to produce an air-clad photonic crystal, but sufficient oxide remained at the edge of the device to anchor the structure to the substrate. Fig. 1a shows SEM images of a fabricated photonic crystal device.

For the quantum-dot fabrication and deposition, a close-packed PbS quantum-dot monolayer was created using evaporation-induced nanoparticles/polymer self-assembly [35]at a fluid interface, followed by monolayer transfer as recently reported[36]. Because the monolayer has a high modulus, it remains freely suspended over air holes without adhering to the side walls. A TEM image of the QD film on a TEM grid is shown in the inset of Fig. 1d.

The close-packing gives a QD density of 10^4 μm^{-2}, which is over two orders of magnitude higher than typical with Stranski-Krastanow growth. The density and uniformity are sufficiently high to relax the requirement of matching QD locations to the antinode region of the cavity mode. Moreover, colloidal QDs provide greater material and functionality flexibilities. Incorporation of QD can occur during post-processing, under ambient conditions using self-assembly of ligand functionalized QDs[23, 35, 37]. These quantum dots are purchased from Evident Technologies.

For measuring the photoluminescence (PL) of the excited QDs, we used a standard micro-PL setup where the excitation source and PL signal are focused and collected through 0.65NA Mitutoyo 50X NIR HR microscope objective. This objective has a collection efficiency of 42% of the upper hemisphere. The field of view of the detection optics has about a 15 μm diameter. The excitation source is a cw 830nm or 904nm diode laser delivered by a single-mode 5.6μm core fiber collimated to match the entrance pupil of the objective. We have not notice any significant difference in the enhancement factor when switching between these two laser sources. However, 904nm laser appears to have a smaller photo-bleaching effect. A diffraction limited spot size of ca. 1.6μm $1/e^2$ diameter is produced on the sample. The out-of-plane PL is collected by the same objective and coupled to a 0.3m or 0.5m imaging spectrometer through a 50um diameter multimode fiber with a spectral resolution of 0.4nm and 0.1nm respectively equipped with an OMAV InGaAs array detector.

3. Optical measurements

3.1 Spectroscopy of microcavity resonances

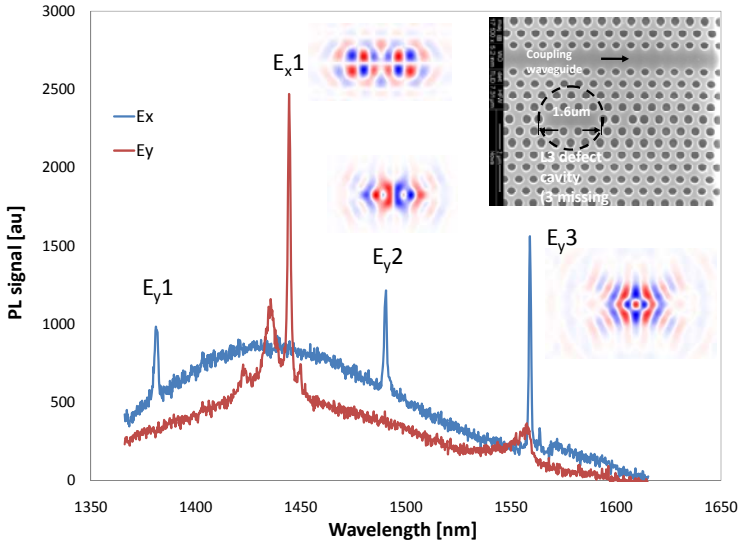

Fig. 2. Measured photoluminescence (PL) spectrum taken from the same L3 cavity with polarization parallel (E_x) and perpendicular (E_y) to the long axis of the cavity. The calculated modal patterns are shown next to resonance peaks. The inset shows the excitation spot size relative to the cavity.

Emission is mostly from the ground-state transition, involving states populated via collisional relaxation from higher lying levels in a picosecond time scale [38]. In fact, the PL signal is independent of the excitation polarization is consistent with this pump relaxation dynamics [39]. However, the PL from the cavity resonance is highly polarized and is present only when the quantum dots on the cavity are excited. The wavelengths of the resonances are expected to be slightly different from sample to sample due to variation in the polymer film thickness, but their relative positions are very reproducible and in agreement with Finite Difference Time Domain (FDTD) calculations. We have used both poly-3 hexylthiophene (P3HT) and polystyrene (PS) polymer for the deposition and the difference in performance is relatively minor. A typical emission spectrum is shown in Fig. 2. Using PS, the highest Q factor observed from the E_y3 resonance is greater than 8000. The broad background emission is from quantum dots that are either not coupled to the cavity or outside the cavity region excited by the laser. This emission is very similar to the one obtained from a free-standing film (free-film). The feature on the red trace at 1560nm is the $1.1W_1$ waveguide mode. The small features on the short wavelength side of the E_x1 resonance are hybridized modes caused by the coupling between the waveguide and the cavity. This coupling apparently has no effect on the E_y resonances.

Table 1: **Calculated and measured wavelengths and Q factors of cavity resonances. E // WG means the electric field polarization of the PL is parallel to the waveguide (WG) and E X WG means the polarization of the PL is perpendicular to the WG**.

$\omega a/2\pi c$	Identification	λ (*expt*/cal)	Q_{max} (*expt*/cal)	Experimental uncertainty (nm)
E X WG	Ex1	*1457.9*/1455.04	*600*/416	+/- 3
E // WG	Ey1	*1399*/1396	*720*/1214	+/- 10
E // WG	Ey2	*1512.44*/1511.7	*1257*/2182	+/- 11
E // WG	Ey3	*1580.74*/1582.7	*8028*/16108	+/- 9

For the photonic crystal bandstructure, wavelengths of micro-cavity resonances, and Q factors calculations, we use the MIT Electromagnetic Equation Propagation (MEEP) simulation environment[40]. The photonic crystal structure including the polymer film is discretized into a three dimensional computational supercell of 20 x 16 x 20 periods. Quantum-dot emission is simulated by an arrangement of multiple point current sources covering the waveguide and L3 cavity. For each point source, we use a Gaussian pulse centered at a reduced frequency of 0.273 (in unit of $c/2\pi a$) with a frequency spread of 0.05. To account for the existence of a bandgap in the transverse electric (TE) polarization of the L3 structure, the current sources are oriented in the z direction. Computation of the eigenmodes together with their quality factors (Q) were performed with the harmonic inversion technique [41], which determines the resonant frequencies, decay constants, amplitudes, and phases of sinusoids composing a discretized time signal. Unlike the more commonly used Fourier transform, harmonic inversion describes the signal using an adaptive, finite length series of decaying and non-decaying sinusoids. The respective time series of the electric components for use with harmonic inversion were detected in the far field at 8 periods (computational unit cells) away from the sources to match the detection condition in the laboratory. These time series were later processed via the harmonic inversion method to identify the resonant modes. For the Q factor and modal field calculations, we use a narrower (than quantum dot emission) bandwidth for the point sources and tune the emission frequency around the neighborhood of the mode resonances. The modal patterns for E_x1, E_y2 and E_y3 are shown in Fig. 2. The quantitative agreement between theory and experiment is to within 1.5% in the resonant frequencies as summarized in Table 1. For the E_x1 resonance, the measured Q factor is higher than the calculated value. The cause may be due to the sensitivity of the cavity geometry, so that very slight differences between input and actual cavity parameters result in noticeable discrepancies. Examples of sensitive parameters include side-wall straightness, hole locations and diameters [34]. In addition, the integrated PL signal from the cavity-free patterned region is comparable to that obtained from a free-standing film, indicating that the photoluminescence signal is not being trapped or scattered outside the field of view of the detection system.

3.2 Angular distribution measurements

In order to be able to determine the enhancement factor of the emission, it is necessary to normalize the cavity-resonance emission to the emission in the absence of cavity influences. We chose emission from a free-standing film with monolayer of close-packed quantum dots

(free-film) as the reference because 1) the angular distribution from the film is garanteed to obey the cosine law; 2) the PL intensity is very stable and uniform to within 20%. While the emission from the cavity-free patterned region is typically used as a reference in other work [20], we find this to be less reliable because the angular distribution is not a cosine law distribution and it can be affected by any buckling of the photonic crystal membrane structure. The two measured angular distributions are shown in Fig. 4. In addition, the intensity from the cavity-free pattern region can depend on the quality of film contact to the photonic crystal surface.

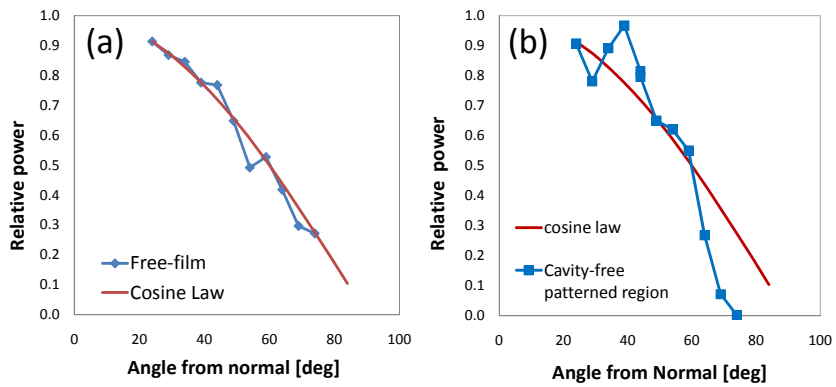

Fig. 4. Measured angular distribution of photoluminescence from a free-film (a), and cavity-free patterned region (b) with a monolayer of close-packed quantum dots. All data are normalized to the value of cos(24°), which is the smallest angle the apparatus can measure. The inset of (b) is the calculated angular distribution.

As shown in Fig. 5, a coarse measure of the angular behaviors and collection efficiencies of the cavity resonances is possible using different numerical aperture focusing/collection objectives corrected for the transmission of the pump and signal wavelengths. The PL signals from 20x and 10x objectives are normalized to the collection efficiency value of 0.42 of 50x objective if it were a Lambertian source. To ensure this methodology is correct, we use the emission from a free-standing film (free-film) as a test case and obtained the expected Lambertian behavior. From these measurements, we determined that the emission from the free-film and anchor (pattern-free) regions have very similar behavior. Both E_x1 and E_y2 resonances do not have emission intensity peaked toward the normal direction due to significantly weaker signal than the Cosine law distribution when the 10x objective was used. These behaviors are consistent with the angular distributions obtained from numerical simulations shown in the insets of Fig 5c and 5d. Using an objective with a numerical aperture of 0.15, the excitation spot size is much larger than the cavity area, the PL signal is overwhelmed by the contribution outside of the cavity area and therefore no cavity resonance emission was discernable. Most importantly, none of these emissions show a very directive behavior which can render gross errors in the enhancement factor estimates discuss later.

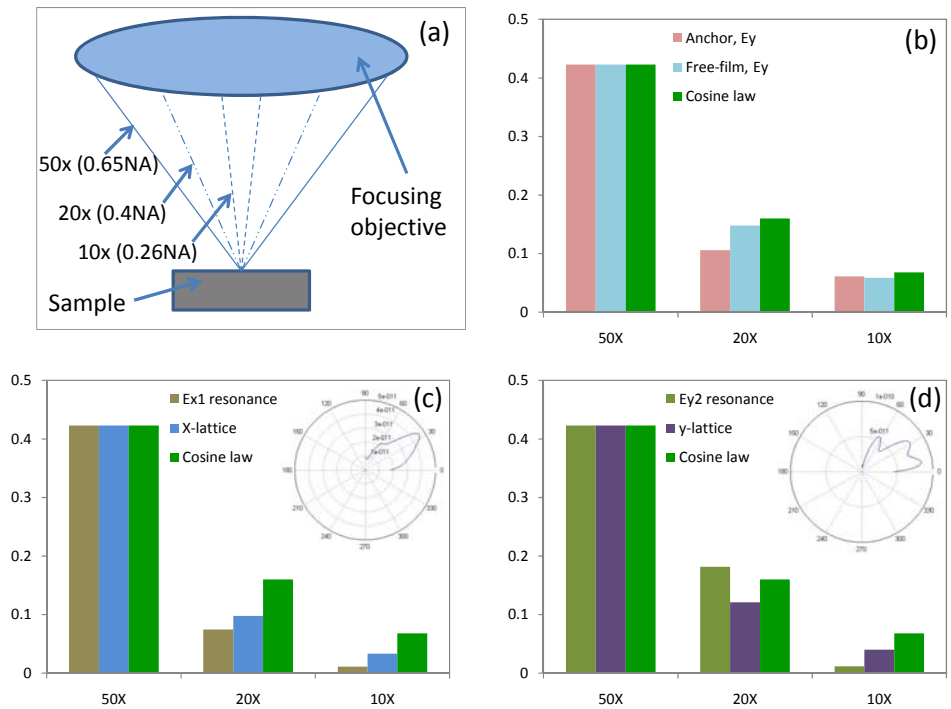

Fig. 5. A schematic drawing depicts the collection geometries of different numerical aperture (NA) objectives (a). The PL signals from 20x and 10 objectives are normalized to the Lambertion collection efficiency valued 0.42 for 50x objective. The relative collection efficiency behaviors of the PL from free-film, anchor region and the Cosine law (b) show minor deviation from the Cosine law behavior. The relative collection efficiencies of E_x1 (c) and E_y2 (d) resonances using 10x objective are much smaller than Cosine law behavior indicating the emissions directed away from normal in agreement with simulation results (insets).

3.2 Enhanced emission from the Fabry-Perot-like waveguide resonances

Along the y direction, the waveguide can be viewed as a Fabry-Perot (FP) cavity bounded by two photonic lattice mirrors. The propagation vector of the FP cavity modes is along the y direction, and therefore its electric field is along the x direction. When the excitation source is focused on the waveguide, enhanced emission along x polarization is observed shown in Fig. 6. This emission is 12 times larger than that of the free-standing film. As we expect, no resonance is observed in the y polarization. The background emission arises from the emitters not coupled to the FP cavity resonance and scattered to free-space whereas the enhanced emission is scattered into the free space as the dominant loss mechanism. The excitation area is defined by the excitation spot diameter along x direction and the width of the waveguide in the y direction, therefore this area is comparable to the L3 microcavity. The mode volume however is quite large because there is no mode confinement in the y direction. Correcting for excitation area that can couple to the waveguide (area ratio = 5), the emission rate is approximately 50 times larger than free film even if one assume 100% collection efficiency[42]. Because of the low Q factor (200) and large mode volume, Purcell effect enhancement factor is negligible. It is known that the presence of high refractive index material can also enhance emission rate due to n^3 dependence in photonic density of states. Although the vacuum field amplitude is reduced by a factor of n by conventional macroscopic polarization consideration, the net emission rate is enhanced by a factor of n [43-45]. To include the local field effect, the spontaneous emission rate of a dipole in a dielectric medium is given as $\Gamma_D = (nL^2)\Gamma_{vac}$, where Γ_D and Γ_{vac}

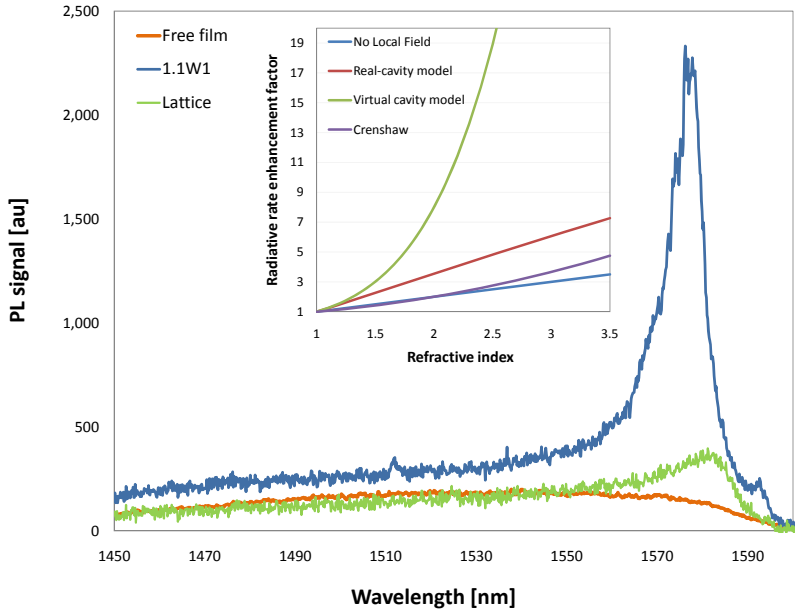

Fig. 6. Enhanced emission from the Fabry-Perot-like resonance of the 1.1W$_1$ waveguide, free film and lattice regions. Subtracting the peak signal from the background at 1530nm, the enhancement factor with respect to the free film without area correction is 12. The inset shows the dielectric enhancement factor for different index enhancement models.

are the decay rates of an emitter in a dielectric and vacuum respectively, L is the local field enhancement factor. In the absence of local field enhancement (L=1), the enhancement factor from the dielectric effect is n. There are many local field models: for the real-cavity model, $L=(3n^2)/(2n^2+2)$ [46]; virtual cavity, $L=(n^2+2)/3$[44, 47]; and the Crenshaw model, $L=((n^2+2)/3n)^{1/2}$ [48]. Experimental studies in the index range of 1.3-1.7 have shown agreement with the real cavity model. Based on the real cavity model for silicon, a significant dielectric enhancement factor $EF_D=nL^2=7.3$ is obtained.

To determine quantitatively the enhancement factor, the emitter area (A), enhanced

Table 2: **Estimated enhanced emission factor based on dielectric enhancement only.**

	A	EF_A	EF_D	EF_{cav}	β	η_{FS}	η_C	S	Measured ratio
Free-film	1	1	1.8	n/a	n/a	1	0.42	1	
1.1W$_1$ Resonance	0.2	1.3	7.3	1.0	1	1	1	1.54	8-12
Ex1 Resonance	0.16	1.3	7.3	1.0	1	1	0.45	0.72	8-16

absorption factor (E_A), dielectric enhancement (EF_D), Purcell cavity effect enhancement (EF_{cav}), coupling strength to the photonic crystal cavity (β), coupling strength to the free-space from the cavity (η_{FS}), and collection efficiency (η_C) need to be included. Therefore, we write the expected signal (S) as

$S = A \cdot E_A \cdot EF_D \cdot EF_{cav} \cdot \beta \cdot \eta_{FS} \cdot \eta_C$, and the values in this expression for the free-film and FP resonances are shown in Table 2.

An enhanced absorption factor E_A=1.3 is present when the quantum dots resides on the surface of Si because significant reflectivity from silicon provides another pass to excite the quantum dots again. The dielectric enhancement factor for free film is 1.8 with respect to a truly free quantum dot in vacuum. Assuming 100% collection efficiency, the observed enhancement factor is significantly larger than this estimate.

3.3 Enhanced emission from microcavities

As discussed before, we use free-film emission as the reference. The enhancement factor is determined by taking the magnitude of the emission peak above the background and dividing by the free-film emission at the same wavelength. The enhancement factors for E_x1, E_y1, E_y2 and E_y3 are shown in Fig. 7. The data shown are composed of measurements performed on different samples using both P3HT and PS polymer. Notice that the expected linear dependence of the enhancement factor on Q due to the Purcell effect is absent confirming that PbS belongs to the "bad emitter" class. While the exact value of the homogenous linewidth of PbS is still under debate, based on our low temperature 105K measurements, the emission linewidth is 26meV. Other single quantum dots measurements of PbS emitting at 800nm, the homogenous width was determined to be 100meV [32]. We believe the actual homogenous width of 1500nm emitting dot is significantly less than 26meV because our measurements were not performed on a single dot and therefore this width includes inhomogenous broadening. In addition, the spectral diffusion effect will also contribute additional broadening.

Since the index of refraction of free-film is different from the cavity, the expression for the enhancement factor for cavities with respect to the free-film is given by

$$\Gamma_{D-cav} = \Gamma_D \left(\frac{(\lambda / n_c)^3}{V} \right) \left(\frac{\omega_{emitter}}{\Delta\omega_{emitter}} \right) \left(\frac{L_c^2}{L^2} \right) \left(\frac{n_c}{n} \right) \left(\frac{1}{4\pi^2} \right)$$

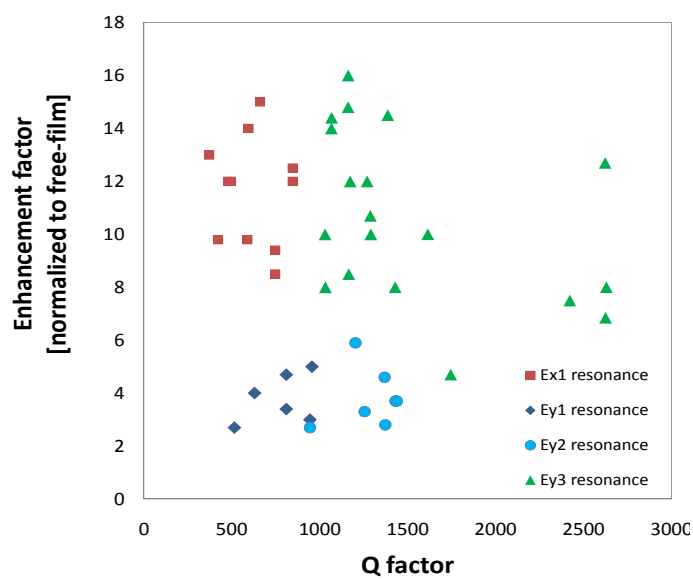

Fig. 7. Measured enhancement factor of E_x1, E_y2, and E_y3 microcavity resonances with respect to the free-film. The enhancement factor is determined by the height of the resonance above the background emission divided by the emission of a free-standing film at the resonant frequency. The effect of excitation area to the cavity area is not included.

where $\Gamma_{D\text{-}cav}$ and Γ_D are radiative rate of the emitter in a dielectric cavity and free standing polymer film respectively, $\omega_{emitter}$ and the $\Delta\omega_{emitter}$ are the central frequency and its homogenous width respectively [26].

In the case of the cavity emission, the area of the cavity is 6 times smaller than the excitation area with a mode volume of $0.95(\lambda/n)^3$ based on FDTD simulations. The Purcell enhancement factor is 0.75 upon averaging the polarization orientation and using the measured emitter Q of 30. However, the dielectric enhancement is the same as discussed earlier. The β coupling factor for the cavity emission is generously taken to be 1. This is reasonable given the large dielectric enhancement factor. In addition, recent numerical simulations also support this behavior [49]. Any value less than 1 would require larger enhancement factor to produce the observed signature. For the free-film case, this factor is not relevant because the thickness of the film is too thin to support any trapped modes. Furthermore, η_{FS} is taken to be 1 for the free film and microcavity, because within the Q factors range being discussed, the photon lifetime is too short to incurr significant absorption. The collection efficiency for E_x1 cavity mode is 0.45 based on our FDTD simulation,

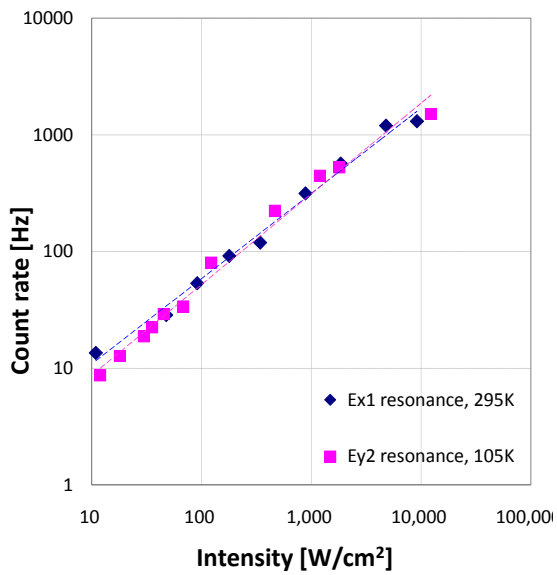

Fig. 8. Intensity dependent behavior of E_x1 at 295K and E_y2 at 105K resonances. Both exhibit sub-linear intensity dependence of the form $y=ax^b$, where b=0.73 and 0.78 for E_x1 and E_y2 resonances respectively.

whereas for the free-film, it is 0.42 because the source is lambertian following the Cosine distribution which has been verified from our angular distribution measurements shown in Fig. 5. Using these values, we determined that the observed enhancement factor is more than 10 times larger than this estimate. Since the observed enhancement factors for waveguide and microcavity are very similar, the Purcell effect enhancement must be negligible.

A remaining concern is whether the observed emission enhancement is actually from amplified spontaneous emission. To address this question, we performed intensity dependence studies and found three pieces of evidence to preclude this effect. First, with a change in excitation intensity from 10 W/cm^2 to 10^4 W/cm^2, we did not find an increase in slope in the emission intensity versus excitation intensity, which would indicate a transition from spontaneous emission to amplified spontaneous emission (Fig. 8). In fact, they all show

sub-linear behavior which can fit to a power law dependence of $y=ax^b$ very well; with b=0.73 for the E_x1 resonance at room temperature and b=0.78 for the E_y2 resonance at 105K. This sub-linear behavior[50] is commonly observed in colloidal quantum dots photoluminescence and is believed to be associated with the quantum dot blinking problem where quantum dot can be charged or carriers are trapped on the surface[51]. Second, the ratio between each emission peak and the background remains constant to within <20% over the same 3 orders of magnitude change excitation intensities, there is no spectral redistribution upon change in pump intensity. Third, we observed no linewidth narrowing effect for E_x1, E_y2 and E_y3 resonances.

4. Discussion and conclusion

We observed a more than 50 fold enhancement in the emission from both Fabry-Perot-like waveguide and microcavity resonances. Since the dielectric enhancement effect can only account for a factor of 7.3, there remains a significant factor enhancement factor that cannot be accounted for. One may speculate that the excited quantum dots outside the cavity or waveguide region can transfer their energies to those in resonance with the cavity mode by non-radiative dipole-dipole interaction [52-53] given the fact that the separation between quantum dots is only 1-2nm apart. Resonant energy transfer may effectively enlarge the excitation area because on average quantum dots that are resonant to the cavity spend more time as un-excited dots and therefore act as acceptors, whereas the the off-resonance ones are inhibited from emission due to lack of photonic states are likely to be donors. This effect will be investigated in future work. Conclusive confirmation of the enhancement factor requires lifetime measurements of emitters in these structures, and presently, this measurement is not feasible. However, if a non-radiative energy transfer mechanism is present, this will not be manifestated in the lifetime measurements.

Acknowledgments

The authors acknowledge fruitful discussion with R. Kekatpure and Mike Sinclair, numerical simulations from I. El-Kady, B.G. Farfan and M.R. Taha, and fabrication support from the staff at the Microelectronics Development Laboratory (MDL) at Sandia National Laboratories (SNL). Support for this work is from SNL's Laboratory Directed Research Development (LDRD) program and by the U. S. Department of Energy through the Office of Science, Office of Basic Energy Sciences (BES), and Energy Frontier Research Center (EFRC) for Solid-State Lighting Science and Center for Integrated Nanotechnologies (CINT, national user facility). SNL is a multi-program laboratory operated by Sandia Corporation, a part of Lockheed-Martin Corporation, for the U. S. Department of Energy under Contract No. DE-AC04-94AL85000.

1. K. J. Vahala, "Optical microcavities," Nature **424**, 839-846 (2003).
2. J. Wiersig, C. Gies, F. Jahnke, M. Aszmann, T. Berstermann, M. Bayer, C. Kistner, S. Reitzenstein, C. Schneider, S. Hofling, A. Forchel, C. Kruse, J. Kalden, and D. Hommel, "Direct observation of correlations between individual photon emission events of a microcavity laser," Nature **460**, 245-249 (2009).
3. M. Pelton, C. Santori, J. Vuckovic, B. Zhang, G. S. Solomon, J. Plant, and Y. Yamamoto, "Efficient source of single photons: a single quantum dot in a micropost microcavity," Phys Rev Lett **89**, 233602 (2002).

4. C. Santori, D. Fattal, J. Vuckovic, G. S. Solomon, and Y. Yamamoto, "Indistinguishable photons from a single-photon device," Nature **419**, 594-597 (2002).
5. B. Lounis, and M. Orrit, "Single-photon sources," Reports on Progress in Physics **68**, 1129-1179 (2005).
6. G. Khitrova, H. M. Gibbs, M. Kira, S. W. Koch, and A. Scherer, "Vacuum Rabi splitting in semiconductors," Nat Phys **2**, 81-90 (2006).
7. A. J. Shields, "Semiconductor quantum light sources," Nat Photon **1**, 215-223 (2007).
8. P. Michler, A. Imamoglu, M. D. Mason, P. J. Carson, G. F. Strouse, and S. K. Buratto, "Quantum correlation among photons from a single quantum dot at room temperature," Nature **406**, 968-970 (2000).
9. M. Makarova, J. Vuckovic, H. Sanda, and Y. Nishi, "Silicon-based photonic crystal nanocavity light emitters," Applied Physics Letters **89** (2006).
10. T. Tanabe, K. Nishiguchi, E. Kuramochi, and M. Notomi, "Low power and fast electro-optic silicon modulator with lateral p-i-n embedded photonic crystal nanocavity," Opt. Express **17**, 22505-22513 (2009).
11. J. M. Phillips, P. E. Burrows, R. F. Daves, J. A. Simmons, G. G. Malliaras, F. So, M. J.A., A. V. Nurmikko, and D. L. Smith, "Basic research needs for solid-state lighting," (2006).
12. M. Ji, S. Park, S. T. Connor, T. Mokari, Y. Cui, and K. J. Gaffney, "Efficient Multiple Exciton Generation Observed in Colloidal PbSe Quantum Dots with Temporally and Spectrally Resolved Intraband Excitation," Nano Lett. **9** (2009).
13. T. Tiedje, E. Yablonovitch, G. D. Cody, and B. G. Brooks, "Limiting efficiency of silicon solar cells," Ieee Transactions on Electron Devices **ED-31** (1984).
14. A. Kress, F. Hofbauer, N. Reinelt, M. Kaniber, H. J. Krenner, R. Meyer, G. Bohm, and J. J. Finley, "Manipulation of the spontaneous emission dynamics of quantum dots in two-dimensional photonic crystals," Physical Review B **71** (2005).
15. T. Lund-Hansen, S. Stobbe, B. Julsgaard, H. Thyrrestrup, T. Sunner, M. Kamp, A. Forchel, and P. Lodahl, "Experimental Realization of Highly Efficient Broadband Coupling of Single Quantum Dots to a Photonic CrystalWaveguide," Phys Rev Lett **101** (2008).
16. M. Nomura, N. Kumagai, S. Iwamoto, Y. Ota, and Y. Arakawa, "Photonic crystal nanocavity laser with a single quantum dot gain," Optics Express **17** (2009).
17. I. Fushman, D. Englund, A. Faraon, N. Stoltz, P. Petroff, and J. Vuckovic, "Controlled phase shifts with a single quantum dot," Science **320**, 769-772 (2008).
18. A. Faraon, I. Fushman, D. Englund, N. Stoltz, P. Petroff, and J. Vuckovic, "Coherent generation of non-classical light on a chip via photon-induced tunnelling and blockade," Nature Physics **4**, 859-863 (2008).
19. I. Fushman, D. Englund, and J. Vuckovic, "Coupling of PbS quantum dots to photonic crystal cavities at room temperature," Applied Physics Letters **87** (2005).
20. M. Fujita, Y. Tanaka, and S. Noda, "Light emission from silicon in photonic crystal nanocavity," Ieee Journal of Selected Topics in Quantum Electronics **14**, 1090-1097 (2008).
21. Z. Wu, Z. Mi, P. Bhattacharya, T. Zhu, and J. Xu, "Enhanced spontaneous emission at 1.55 mu m from colloidal PbSe quantum dots in a Si photonic crystal microcavity," Applied Physics Letters **90** (2007).
22. M. Makarova, V. Sih, J. Warga, R. Li, L. Dal Negro, and J. Vuckovic, "Enhanced light emission in photonic crystal nanocavities with erbium-doped silicon nanocrystals (vol 92, art no 161107, 2008)," Applied Physics Letters **92** (2008).

23. A. G. Pattantyus-Abraham, H. Qiao, J. Shan, K. A. Abel, T.-S. Wang, F. C. J. M. van Veggel, and J. F. Young, "Site-Selective Optical Coupling of PbSe Nanocrystals to Si-Based Photonic Crystal Microcavities," Nano Letters **9**, 2849-2854 (2009).
24. J. Yang, J. Heo, T. Zhu, J. Xu, J. Topolancik, F. Vollmer, R. Ilic, and P. Bhattacharya, "Enhanced photoluminescence from embedded PbSe colloidal quantum dots in silicon-based random photonic crystal microcavities," Applied Physics Letters **92**, 261110-261111-261110-261110-261113 (2008).
25. Y. Gong, M. Makarova, S. Yerci, R. Li, M. J. Stevens, B. Baek, S. W. Nam, R. H. Hadfield, S. N. Dorenbos, V. Zwiller, J. Vuckovic, and L. Dal Negro, "Linewidth narrowing and Purcell enhancement in photonic crystal cavitieson an Er-doped silicon nitride platform," Opt. Express **18**, 2601-2612 (2010).
26. A. Meldrum, P. Bianucci, and F. Marsiglio, "Modification of ensemble emission rates and luminescence spectra for inhomogeneously broadened distributions of quantum dots coupled to optical microcavities," Opt. Express **18**, 10230-10246 (2010).
27. H. Y. Ryu, and M. Notomi, "Enhancement of spontaneous emission from the resonant modes of a photonic crystal slab single-defect cavity," Optics Letters **28**, 2390-2392 (2003).
28. Y. Xu, R. K. Lee, and A. Yariv, "Finite-difference time-domain analysis of spontaneous emission in a microdisk cavity," Physical Review A **61**, 033808 (2000).
29. M. Makarova, V. Sih, J. Warga, R. Li, L. Dal Negro, and J. Vuckovic, "Enhanced light emission in photonic crystal nanocavities with erbium-doped silicon nanocrystals," Applied Physics Letters **92** (2008).
30. J. M. Harbold, and F. W. Wise, "Photoluminescence spectroscopy of PbSe nanocrystals," Physical Review B (Condensed Matter and Materials Physics) **76** (2007).
31. L. Turyanska, A. Patane, M. Henini, B. Hennequin, and N. R. Thomas, "Temperature dependence of the photoluminescence emission from thiol-capped PbS quantum dots," Applied Physics Letters **90**, 101913-101913 (2007).
32. J. J. Peterson, and T. D. Krauss, "Fluorescence Spectroscopy of Single Lead Sulfide Quantum Dots," Nano Letters **6**, 510-514 (2006).
33. S. Xiong, X. Miao, J. Spencer, C. Khripin, T. S. Luk, and C. J. Brinker, "Integration of a Close-Packed Quantum Dot Monolayer with a Photonic-Crystal Cavity Via Interfacial Self-Assembly and Transfer," Small, n/a-n/a (2010).
34. Y. Akahane, T. Asano, B. S. Song, and S. Noda, "High-Q photonic nanocavity in a two-dimensional photonic crystal," Nature **425** (2003).
35. J. Pang, S. Xiong, F. Jaeckel, Z. Sun, D. Dunphy, and C. J. Brinker, "Free-Standing, Patternable Nanoparticle/Polymer Monolayer Arrays Formed by Evaporation Induced Self-Assembly at a Fluid Interface," Journal of the American Chemical Society **130**, 3284-3285 (2008).
36. S. Xiong, X. Miao, J. Spencer, C. Khripin, T. S. Luk, and C. J. Brinker, "Integration of a close-packed quantum dot monolayer with a photonic-crystal cavity via interfacial self-assembly and transfer," Small **to be published.** (2010).
37. H. Fan, K. Yang, D. M. Boye, T. Sigmon, K. J. Malloy, H. Xu, G. P. López, and C. J. Brinker, "Self-Assembly of Ordered, Robust, Three-Dimensional Gold Nanocrystal/Silica Arrays," Science **304** (2004).
38. R. D. Schaller, J. M. Pietryga, S. V. Goupalov, M. A. Petruska, S. A. Ivanov, and V. I. Klimov, "Breaking the Phonon Bottleneck in Semiconductor Nanocrystals via

Multiphonon Emission Induced by Intrinsic Nonadiabatic Interactions," Physical Review Letters **95**, 196401 (2005).
39. J. M. An, M. Califano, A. Franceschetti, and A. Zunger, "Excited-state relaxation in PbSe quantum dots," Journal of Chemical Physics **128** (2008).
40. J. D. Joannopoulos, S. G. Johnson, J. N. Winn, and R. D. Meade, *Photonic crystals Molding the Flow of Light* (2008).
41. V. A. Mandelshtam, and H. S. Taylor, "Harmonic inversion of time signals and its applications," Journal of Chemical Physics **107**, 6756-6769 (1997).
42. N.-V.-Q. Tran, Combri, eacute, Sylvain, and A. De Rossi, "Directive emission from high- Q photonic crystal cavities through band folding," Physical Review B **79**, 041101 (2009).
43. M. E. Crenshaw, "The quantized field in a dielectric and application to the radiative decay of an embedded atom," Physics Letters A **358**, 438-442 (2006).
44. K. Dolgaleva, R. W. Boyd, and P. W. Milonni, "Influence of local-field effects on the radiative lifetime of liquid suspensions of Nd:YAG nanoparticles," J. Opt. Soc. Am. B **24**, 516-521 (2007).
45. P. R. Berman, and P. W. Milonni, "Microscopic Theory of Modified Spontaneous Emission in a Dielectric," Physical Review Letters **92**, 053601 (2004).
46. R. J. Glauber, and M. Lewenstein, "Quantum optics of dielectric media," Physical Review A **43**, 467 (1991).
47. H. A. Lorentz, *Theory of electrons* (Teubner, 1916).
48. M. E. Crenshaw, and C. M. Bowden, "Effects of Local Fields on Spontaneous Emission in Dielectric Media," Physical Review Letters **85**, 1851 (2000).
49. K. R. Catchpole, and A. Polman, "Plasmonic solar cells," Optics Express **16** (2008).
50. V. I. Klimov, A. A. Mikhailovsky, S. Xu, A. Malko, J. A. Hollingsworth, C. A. Leatherdale, H. J. Eisler, and M. G. Bawendi, "Optical gain and stimulated emission in nanocrystal quantum dots," Science **290**, 314-317 (2000).
51. S. Liao, M. Dutta, D. Schonfeld, T. Yamanaka, and M. Stroscio, "Quantum dot blinking: relevance to physical limits for nanoscale optoelectronic device," Journal of Computational Electronics **7**, 462-465 (2008).
52. S. W. Clark, J. M. Harbold, and F. W. Wise, "Resonant energy transfer in PbS quantum dots," Journal of Physical Chemistry C **111**, 7302-7305 (2007).
53. G. D. Scholes, and G. Rumbles, "Excitons in nanoscale systems," Nat Mater **5**, 683-696 (2006).

4. Ultra-small volume plasmonic nanocavity for enhancing quantum dot emission

In this section, we describe an approach to enhance spontaneous emission using plasmonic nanocavity and possible method to make this type of cavities with high degree of mono-dispersity.

Nanocomposite plasmonic fluorescence emitters with core/shell configurations

Xiaoyu Miao,[1,2,*] Igal Brener,[1,2] and Ting Shan Luk[1,2]

[1]*Sandia National Laboratories, P.O. Box 5800, Albuquerque, New Mexico 87185, USA*
[2]*Center for Integrated Nanotechnologies, Sandia National Laboratories, P.O. Box 5800, Albuquerque, New Mexico 87185, USA*
[*]*Corresponding author: xiaoyu.miao@gmail.com*

Received May 7, 2010; accepted June 7, 2010;
posted June 15, 2010 (Doc. ID 128025); published July 16, 2010

This paper is focused on the optical properties of nanocomposite plasmonic emitters with core/shell configurations, where a fluorescence emitter is located inside a metal nanoshell. Systematic theoretical investigations are presented for the influence of material type, core radius, shell thickness, and excitation wavelength on the internal optical intensity, radiative quantum yield, and fluorescence enhancement of the nanocomposite emitter. It is our conclusion that: (i) an optimal ratio between the core radius and shell thickness is required to maximize the absorption rate of fluorescence emitters, and (ii) a large core radius is desired to minimize the non-radiative damping and avoid significant quantum yield degradation of light emitters. Several experimental approaches to synthesize these nanocomposite emitters are also discussed. Furthermore, our theoretical results are successfully used to explain several reported experimental observations and should prove useful for designing ultra-bright core/shell nanocomposite emitters. © 2010 Optical Society of America

OCIS codes: 240.6680, 260.2510.

1. INTRODUCTION

Plasmonics, a rapidly emerging subdiscipline of nanophotonics, is aimed at exploiting surface plasmons for important applications, including biosensing [1], information processing [1], super-resolution imaging [2], optical manipulation [3], and photovoltaics [4]. Parallel to these research efforts, the possibility to enhance the fluorescence emission using metal nanostructures provides promising routes for creating ultra-bright optical fluorescence emitters, which is critical for improving the signal-to-noise ratio and detection sensitivity of fluorescence microscopy—an essential tool in modern biomedical and clinical applications. The desire to understand and exploit the interaction between metal nanostructures and optical emitters has triggered a large number of investigations over the past decade [5].

The enhancement of fluorescence from various optical emitters such as atoms, molecules, and quantum dots (QDs) by metal nanostructures is based on two mechanisms. One takes place during the optical excitation (absorption) stage and the other one takes place during the light emission stage. First, the incident light interacts with the surface plasmon mode greatly enhancing the optical field. The energy associated with the enhanced surface plasmon field increases the absorption rate of the emitter. Second, the excited emitter subsequently relaxes by emitting energy at the emission wavelength, where the emission rate is enhanced through the Purcell effect [6]. Simultaneously, the emitter also relaxes into non-radiative modes. The observed fluorescence power in far field is proportional to the radiative quantum yield of the nanostructure-emitter system, which is the ratio of the number of photons emitted to the total number of photons absorbed.

We describe here the known derivation of fluorescence enhancement by metal nanostructures. The derivation is based on writing population equations for different energy levels. The incident light excites the light emitter from state $|0\rangle$ (ground state) to state $|1\rangle$ (excited state), with subsequent relaxation to $|i\rangle$ (intermediate state) before decaying back to $|0\rangle$. Under weak illumination condition when the stimulated emission can be neglected, the population equation can be written as

$$N_0 + N_i = N_{\text{all}},$$

$$\frac{\partial N_0}{\partial t} = -\frac{N_0 \sigma_{01,\text{abs}} I_{01}}{\hbar\omega_{01}} + N_i \Gamma_{i0,\text{total}}, \tag{1}$$

where N_0, N_i, and N_{all} are the populations at the states $|0\rangle$, $|i\rangle$, and all levels, respectively; $\sigma_{01,\text{abs}}$ is the absorption cross section of the emitter from $|0\rangle$ to $|1\rangle$; I_{01} is the optical intensity at the absorption frequency ω_{01}; and $\Gamma_{i0,T}$ is the total decay rate from $|i\rangle$ to $|0\rangle$. In the stationary regime $\partial N_0/\partial t = 0$, the population equation gives $N_i \sim |K|^2/\Gamma_{i0,\text{total}}$, where K is the local field enhancement at the absorption frequency and is proportional to $\sqrt{I_{01}}$. The underlying physics is that the excited population is linearly proportional to the optical intensity enhancement and is inversely proportional to the total decay rate. As the fluorescence power from the emitter is proportional to $\Gamma_{i0,\text{rad}} N_i$, where $\Gamma_{i0,\text{rad}}$ is the radiative decay rate from $|i\rangle$ to $|0\rangle$, the power is found to be proportional to the radiative quantum yield $\eta = \Gamma_{i0,\text{rad}}/\Gamma_{i0,\text{total}}$. Therefore, the ratio

0740-3224/10/081561-10/$15.00 © 2010 Optical Society of America

of the fluorescence signal with and without metal nanostructure in the low intensity illumination regime can be determined by

$$\Delta = \frac{P_{rad}}{P_0} = |K(\omega_{01})|^2[\eta(\omega_{i0})/\eta_0(\omega_{i0})], \quad (2)$$

where ω_{i0} is the emission frequency, and η and η_0 are the radiative quantum yields at the fluorescence emission frequency with and without the presence of metal nanostructure, respectively [7,8]. For the second part of the equation, if the enhancement of the radiative decay rate through the Purcell effect is lower than that of the non-radiative decay rate, the radiative quantum yield is decreased—this explains the experimental observation of fluorescence quenching by metal, which typically occurs when the emitter is in very close proximity to the metal [9]. On the contrary, the quantum yield is enhanced when the radiative enhancement exceeds the non-radiative enhancement. This sometimes occurs when the emitter itself has a very low intrinsic quantum yield [10].

Among various types of metal nanostructures used for fluorescence enhancement, a particularly interesting one is the nanocomposite particle with a dielectric core and a metal shell, mainly because of such particles' wide tunable resonant properties and ease of preparation [11]. These particles have been extensively used for surface enhanced Raman scattering [12] and fluorescence enhancement [13] applications. To date, in most of the experiments reported in the literature, the optical emitters locate at the vicinity outside the metal shell [12,13]. This configuration limits the flexibility of integrating the nanoparticle-emitter composite into a cellular system without perturbing cellular functions. In addition, it is challenging to precisely control the emitter location with respect to the metal surface to achieve a fluorescence enhancement effect instead of quenching [14,15].

Recently, a new type of nanocomposite particle configuration was proposed in which the light emitters are embedded inside a metal shell [16]. This configuration has several advantages: (i) the metal shell isolates the encapsulated light emitters from external environment, improving their photostability; (ii) a metal such as gold (Au) is biocompatible, chemically inert, and highly stable, potentially addressing concerns regarding the toxicity of light emitters such as QDs to cells [17]; (iii) the metal surface has been well studied for various types of surface functionalization, and can be conjugated to specific biomolecules [18]; and (iv) there is no critical requirement about the location of the emitter inside the metal shell, as will be discussed in detail in Section 2.

Here we review representative experimental work related to core/shell nanocomposite particles with the light emitters embedded inside. Zhang and co-workers embedded the Raman-active molecules inside the Au-coated silicon dioxide (SiO_2) or titanium dioxide (TiO_2) nanoparticles and showed that an enormous Raman enhancement factor on the order of 10^{10} could be achieved [19,20]. As of fluorescence, both enhancement and quenching were observed by incorporating dye molecules inside the silver (Ag) coated silica beads [21,22]. Very recently, a new type of nanocomposite particle, an Au shell with a QD encapsulated inside, was synthesized by using polyethylene glycol (PEG) chains as the structure scaffold [23]. The Au-QD nanocomposite particles show improved photostability as compared to the original QDs. Nevertheless, the overall fluorescence emission is significantly quenched.

To optimize the design of such core/shell nanocomposite emitters for enhanced fluorescence, it is necessary to thoroughly understand the underlying physics and systematically study the influences of the material and geometric parameters. Previously, Enderlein numerically investigated the influence of the core radius to the fluorescence properties of nanocomposite particles, using the bulk values of the metal's dielectric function [24]. This study neglected the electron-surface collision, which is a significant effect in small metal nanoparticles. More specifically, the dielectric function of a small metal particle becomes size dependent when the metal particle size is much smaller than the mean-free path for bulk metal (38 nm for Au and 57 nm for Ag) [25]. As discussed in detail below, the size dependency of a metal's dielectric function is significant in the size regime of core/shell nanoparticles and will greatly influence the fluorescence properties of the nanocomposite emitter. Therefore, this effect needs to be included to obtain reliable calculation results. Here we include the size effect of metal's dielectric function and use a perturbative approach to evaluate the influence of parameters including material type, core radius, shell thickness, and excitation wavelength on the fluorescence properties of the nanocomposite particle, focusing on how to achieve a high fluorescence enhancement. Specifically, we first calculate the optical intensity enhancement inside the nanoparticle without the light emitter (Section 2). Thereafter, we compute the radiative quantum yield of a fluorescence emitter inside the particle using the finite-difference time domain (FDTD) approach (Section 3). By combining the studies of optical intensity and quantum yield, we obtain the fluorescence enhancement of the nanocomposite emitters in Section 4. In Section 5, we discuss several experimental approaches to synthesize the core/shell nanocomposite emitters and their optical properties. The conclusion is presented in the last section.

2. INTERNAL OPTICAL INTENSITY ENHANCEMENT

The geometry of a core/shell nanoparticle is as shown in Fig. 1. Region 1 is the core and is characterized by a radius r_1 and dielectric function ε_1. The shell has a thickness $h = r_2 - r_1$ and a dielectric function ε_2. The surrounding medium has a dielectric function ε_3. When the size of such a core/shell nanoparticle is much smaller as compared to the light wavelength, the electric field around the nanoparticle is time dependent but does not vary spatially. In this case, the analytical electrostatic solution can be obtained by solving Laplace's equation for the electric potential (quasi-static approximation) [26,27]. The electric field in regions 1, 2, and 3 can be calculated by

$$E_1 = \frac{9\varepsilon_2\varepsilon_3}{\varepsilon_2\varepsilon_a + 2\varepsilon_3\varepsilon_b} E_0(\cos\theta\hat{r} - \sin\theta\hat{\theta}),$$

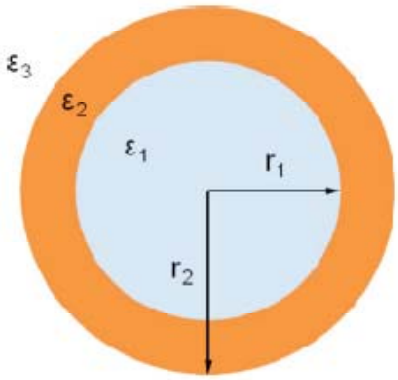

Fig. 1. (Color online) Core/shell nanoparticle geometry: ε_i ($i=1,2,3$) are the dielectric functions of the core, shell, and surrounding medium, respectively; r_1 is the core radius and r_2 is the total particle radius.

$$E_2 = \frac{3\varepsilon_3}{\varepsilon_2\varepsilon_a + 2\varepsilon_3\varepsilon_b}\left\{\left[(\varepsilon_1 + 2\varepsilon_2) + 2(\varepsilon_1 - \varepsilon_2)\left(\frac{r_1}{r}\right)^3\right]E_0 \cos\theta\hat{r} - \left[(\varepsilon_1 + 2\varepsilon_2) - (\varepsilon_1 - \varepsilon_2)\left(\frac{r_1}{r}\right)^3\right]E_0 \sin\theta\hat{\theta}\right\},$$

$$E_3 = \left(2\frac{\varepsilon_2\varepsilon_a - \varepsilon_3\varepsilon_b}{\varepsilon_2\varepsilon_a - 2\varepsilon_3\varepsilon_b}\left(\frac{r_2}{r}\right)^3 - 1\right)E_0 \cos\theta\hat{r} + \left(\frac{\varepsilon_2\varepsilon_a - \varepsilon_3\varepsilon_b}{\varepsilon_2\varepsilon_a + 2\varepsilon_3\varepsilon_b}\left(\frac{r_2}{r}\right)^3 - 1\right)E_0 \sin\hat{\theta}r, \quad (3)$$

where $\varepsilon_a = \varepsilon_1(3-2P) + 2\varepsilon_2 P$, $\varepsilon_b = \varepsilon_1 P + \varepsilon_2(3-P)$, $P = 1 - (r_1/r_2)^3$, and E_0 is the incident electric field. Based on the equations above, it is straightforward to determine the electric field around the core/shell nanoparticle provided that the values of r_1, r_2, ε_1, ε_2, and ε_3 are known.

As aforementioned, the dielectric function of the metal becomes size dependent when the shell thickness is much smaller than the electron mean-free path of the bulk metal. By incorporating the factors representing the electron-surface collision processes, the modified dielectric function of the metal can be determined by

$$\varepsilon(r_1, r_2, \omega) = \varepsilon(\omega)_{bulk} + \frac{\omega_p^2}{\omega^2 + i\omega\gamma_0} - \frac{\omega_p^2}{\omega^2 + i\omega[\gamma_0 + \Delta\gamma(r_1, r_2)]}, \quad (4)$$

where ω_p is the plasma frequency, γ_0 is the bulk collision frequency, and $\Delta\gamma$ is the electron-surface collision frequency. The electron-surface collision frequency is determined by $\Delta\gamma = V_F/\bar{l}$, where V_F is the Fermi velocity and $\bar{l}$ is the electron mean path of the electron-surface collision. For the configuration of the metal shell, we calculate the value of $\bar{l}$ by averaging the length of a random electron free path of the electron-surface collision, either from the inner surface to outer surface or between the outer surfaces. Figures 2(a) and 2(b) compare the bulk values [28] and the size-dependent values of the dielectric function for Au and Ag, respectively. It can be clearly seen that although the real part of the size-dependent dielectric function is almost the same as that of the bulk value, the imaginary part of the size-dependent dielectric function is much larger than that of the bulk value. Such a difference in the imaginary part becomes more significant in the long wavelength regime. Therefore, it is necessary to adopt the size-dependent values of dielectric functions in the calculation for the fluorescence properties of the core/shell nanoparticles.

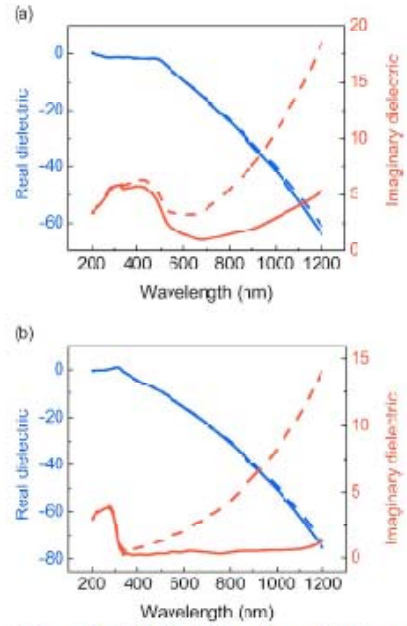

Fig. 2. (Color online) Dielectric functions of (a) Au and (b) Ag. The blue and red curves show the real and imaginary parts of the dielectric function, respectively. The solid and dashed curves show the bulk value and modified value after incorporating the size effect, respectively. Here the core radius and shell thickness of the nanoparticle are assumed to be 5 and 2.5 nm, respectively.

As the first step, we fix the inner and outer radii and examine the wavelength dependence of field intensity enhancement in the core region. The core material is assumed to be SiO_2 with the refractive index of 1.46, the shell material is Au with the size-dependent dielectric function as shown in Fig. 2(a), the surrounding medium is water with the refractive index of 1.33, and the core radius and shell thickness are 20 and 6 nm, respectively. The extinction spectrum of the core/shell nanoparticle is shown as the blue solid curve in Fig. 3(a), which has the resonance peak at 633 nm. Figure 3(a) also plots the optical intensity enhancement in the core region $(E_1/E_0)^2$ as a function of the incident light wavelength (red dashed curve). The maximum of intensity enhancement occurs approximately at the extinction resonance peak. Figure 3(b) shows a cross section of the optical intensity distribution around the core/shell nanoparticle when it is excited at 633 nm. By comparing the optical intensity in the core region and the proximity outside the nanoparticle, there are two findings. First, the enhancement outside the nanoparticle only occurs along the polarization direction of the incident light, while the enhancement in the core region does not have any polarization dependence. Sec-

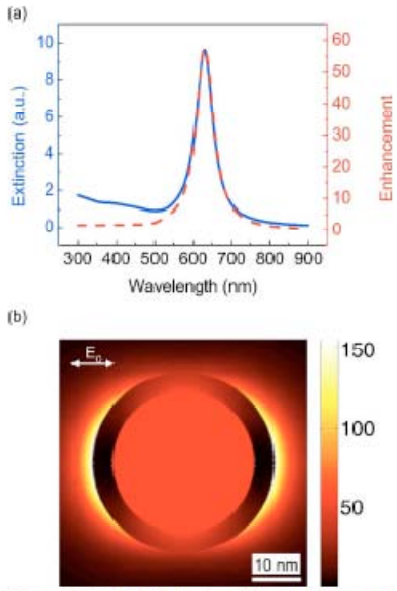

Fig. 3. (Color online) (a) Extinction (blue solid curve) and internal optical intensity enhancement (red dashed curve) of a SiO_2-core Au-shell nanoparticle with the core radius and shell thickness of 20 and 6 nm, respectively. (b) A cross section of the optical intensity distribution around the core/shell nanoparticle when it is excited at 633 nm.

ond, the optical intensity in the core region is much more uniform as compared to that in the outside of the nanoparticle, which decays rapidly with the distance from the surface. Therefore, when a fluorescence emitter locates in the core region, it can experience a substantial enhancement of absorption without requiring critical control of the emitter's location. The emitter can be kept away from the inner metal surface of the nanoparticle to avoid the significant non-radiative damping. However, when a fluorescence emitter is placed outside, although a very high optical intensity enhancement is obtainable in limited regions at the vicinity of the metal surface along the polarization direction of the incident light, fluorescence quenching is likely to occur because the radiative quantum yield is greatly reduced by the strong non-radiative loss in metal.

For a practical fluorescence emitter such as a dye molecule, there is a peak in the emitter's absorption spectrum. To maximize the light absorption of a fluorescence emitter in the core/shell nanoparticle, it is desirable to design the nanoparticle so that the resonant wavelength for optical intensity enhancement coincides with the absorption peak of the emitter. Here we use the Alexa Fluor dyes from Invitrogen [29] as examples to illustrate how to design the geometry of a core/shell nanoparticle in order to maximize the light absorption of a fluorescence emitter. Figure 4 shows the internal optical intensity enhancement as a function of the core radius and shell thickness, with the excitation wavelength located at the absorption peak of each Alexa Fluor dye. Notice that the intensity enhancement for any combination of a core radius and a shell thickness is calculated using the corresponding size-

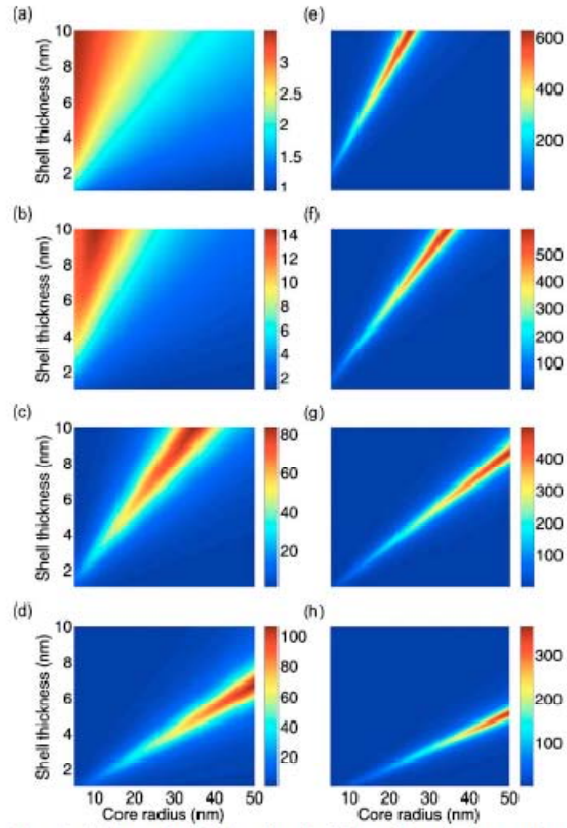

Fig. 4. (Color online) Internal optical intensity enhancement as a function of core radius and thickness when the size-dependent values of the metal's dielectric functions are used. The core material is assumed to be SiO_2. The shell is assumed to be Au for (a)–(d) and Ag for (e)–(h). The excitation wavelengths in (a) and (e), (b) and (f), (c) and (g), (d) and (h) are the absorption peaks of Alexa Fluora 488 (495 nm), Alexa Fluora 532 (532 nm), Alexa Fluora 633 (632 nm), and Alexa Fluora 750 (749 nm), respectively.

dependent dielectric function of metal. An interesting finding is that there is a narrow region associated with a high intensity enhancement in Figs. 4(c)–4(h). This indicates that the optimal design requires the ratio between the shell thickness and core radius to be around a certain value. For instance, the optimal ratio between h and r_1 is approximately 0.3 for Au-shell nanoparticles when the excitation wavelength is 632 nm [Fig. 4(c)]. When the ratio is fixed at the optimal value, larger core radius and shell thickness give a higher intensity enhancement. This is because the electron collision processes are weaker in larger nanoparticles, which leads to a smaller imaginary part of metal's dielectric function and thus less damping effect in intensity enhancement. Another comparison between different shell materials suggests that Ag-shell nanoparticles can generate a much higher intensity enhancement than Au-shell nanoparticles, which is consistent with the fact that Ag is a less lossy material as compared to Au. In addition, Figs. 4(a) and 4(b) show that Au-shell nanoparticles are not effective in generating a high

intensity enhancement when the excitation light has a short wavelength (less than 550 nm).

For the purpose of nanoparticle design, the resonant wavelength for internal optical intensity enhancement as a function of h/r_1 is also calculated. In general, a nanoparticle with a larger value of h/r_1 has the maximum optical intensity enhancement when excited by a shorter wavelength. Figure 5 illustrates such a relationship for different core (Au/Ag) and shell materials (SiO_2/TiO_2). For core/shell nanoparticles with other material configurations, a similar approach can be employed to find the optimal core radius and shell thickness in order to maximize the light absorption of a fluorescence emitter in the nanoparticle.

To illustrate the difference when size-dependent and bulk dielectric functions are used, we also plot in Fig. 6 the internal optical intensity enhancement as a function of the core radius and shell thickness when the bulk dielectric functions are used (the excitation wavelength is fixed at 633 nm). By comparing Fig. 6(a) with Fig. 4(c) for the Au-shell nanoparticle, and Fig. 6(b) with Fig. 4(g) for the Ag-shell nanoparticle, one can see that optical intensity enhancement is overestimated when bulk dielectric functions are used. The large damping as a result of electron-surface collisions significantly reduces the optical intensity enhancement inside the nanoparticle. Therefore, it is necessary to include the size effect of dielectric functions for the investigation of the optical intensity enhancement as well as the radiative quantum yield, which is discussed in the next section.

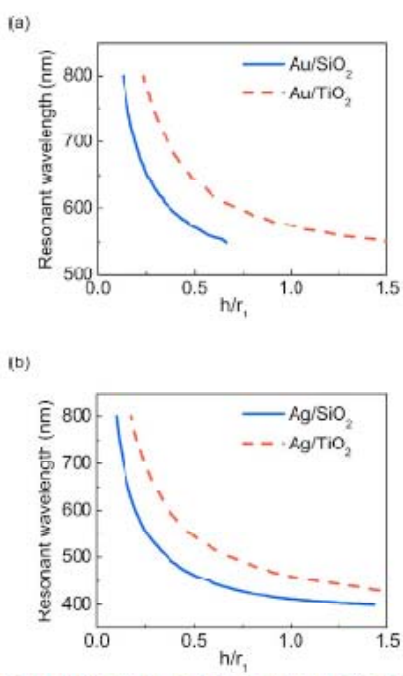

Fig. 5. (Color online) The resonant wavelength for internal optical intensity enhancement as a function of ratio between shell thickness and core radius of (a) Au-shell and (b) silver-shell nanoparticles. The core materials are assumed to be SiO_2 (blue solid curve) and TiO_2 (red dashed curve). The refractive index of TiO_2 (rutile phase) is 2.609.

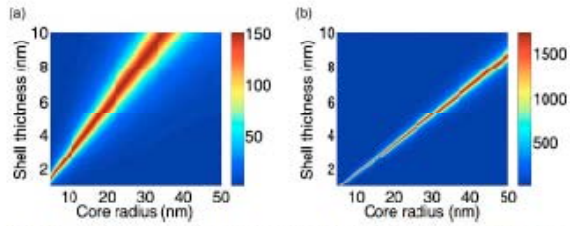

Fig. 6. (Color online) Internal optical intensity enhancement as a function of core radius and thickness when the bulk values of the metal's dielectric functions are used. The excitation wavelength is at 633 nm. The core material is assumed to be SiO_2. The shell is assumed to be Au in (a) and Ag in (b).

3. RADIATIVE QUANTUM YIELD

In this section we provide detailed studies about radiative quantum yield of a fluorescence emitter inside the core/shell nanoparticle. The calculation was performed by FDTD simulation, which discretizes the time-dependent Maxwell's equations using central-difference approximations to the space and time partial derivatives. In our simulation the fluorescence emitter is assumed to be an ideal electric dipole source, which has an infinitely small size and a radiative quantum yield of unity (i.e., every photon absorbed by the emitter results in a photon emitted).

When the dipole source locates inside the core/shell nanoparticle, some of the radiation energy from the dipole will be absorbed by the metal shell and converted into heat. The radiative quantum yield of the nanocomposite emitter is defined as $\eta=\Gamma_{rad}/\Gamma_{total}=\Gamma_{rad}/(\Gamma_{rad}+\Gamma_{nonrad})$, where Γ_{rad}, Γ_{nonrad} and Γ_{total} are the radiative, non-radiative, and total decay rates, respectively. The total decay rate is obtained by computing the total power P_{total} dissipated by the dipole inside the metal shell. The correspondence between quantum and classical theories is valid if the normalized quantities are used [30],

$$\frac{\Gamma_{total}}{\Gamma_{rad,0}}=\frac{P_{total}}{P_0}, \tag{5}$$

where $\Gamma_{rad,0}$ and P_0 are, respectively, the fluorescence decay rate and the radiated power of the dipole source in the homogeneous background environment. The total power P_{total} consists of two parts: radiation power going to the far field P_{rad} and Ohmic loss in the metal shell P_{abs}. The radiative decay rate of the nanocomposite emitter is determined by $\Gamma_{rad}/\Gamma_{rad,0}=P_{rad}/P_0$. The non-radiative decay rate of the nanocomposite emitter is thereby obtained by subtracting the radiative decay rate from the total decay rate.

To compute P_{total} and P_{rad}, we use two sets of monitors in the FDTD simulation, which are closed surfaces on which the flux of the Poynting vector is integrated. One set of monitors takes only the FDTD cell of the dipole source and it implements the calculation of the total power P_{total} radiated by the dipole. The other set of monitors is located outside the core-shell nanoparticle and measures the fluorescence power radiated into the far field P_{rad}. The difference between P_{total} and P_{rad} represents the power being absorbed by the metal shell. This approach can be easily verified by comparing P_{total} and

P_{rad} for a lossless system (without a metal shell): energy conservation implies that the power measured by the two detectors should be equal to each other. The difference between P_{total} and P_{rad} gives an estimate of the numerical error. The numerical error is influenced by a variety of factors including the mesh size and the setting of boundary conditions. In our simulation, the mesh size is set as 0.5 nm; each boundary is set as 64 perfectly matched layers. Such a configuration gives a numerical error smaller than 1% based on the simulation for a lossless system. Here we use the same example as in Fig. 3 and assume that an Alexa Fluor 633 dye molecule with the emission peak at 647 nm is embedded at the center of the core/shell nanoparticle. As shown in Fig. 7(a), both the radiative and non-radiative decay rates of the emitter inside the nanoparticle are significantly enhanced as compared to those of the emitter in the homogeneous background environment. This dramatically reduces the lifetime of the emitter and improves the photostability as the undesired photobleaching only occurs when the emitter is in its excited state [16]. Figure 7(b) shows the radiative quantum yield of the nanocomposite emitter as a function of the emission wavelength. Due to the existence of non-radiative loss in the metal shell, the radiative quantum yield of the nanocomposite emitter is equal to 0.41 at the emission peak (647 nm).

For the next step, we evaluate the dependency of radiative quantum yield of the nanocomposite emitter on the core radius and shell thickness of the nanoparticle, when the emission wavelength is fixed at 647 nm. For the sake of simplification, we still assume that the emitter is located at the center of the particle. As shown in Fig. 8(a),

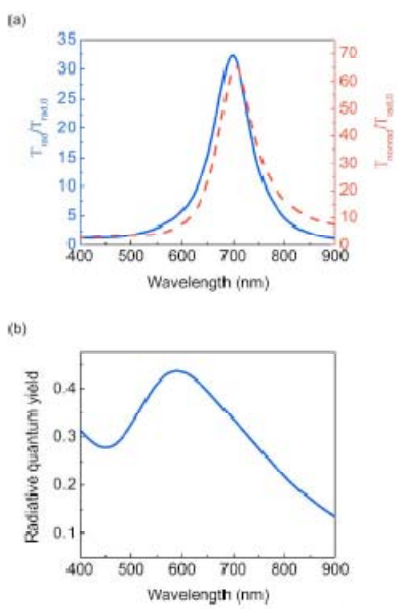

Fig. 7. (Color online) (a) Enhancement of radiative (blue solid curve) and non-radiative (red dashed curve) decay rates, and (b) radiative quantum yield of the nanocomposite emitter. Here an Alexa Fluora 633 dye molecule is assumed to be at the center of a SiO_2-core Au-shell nanoparticle with the core radius and shell thickness of 20 and 6 nm, respectively.

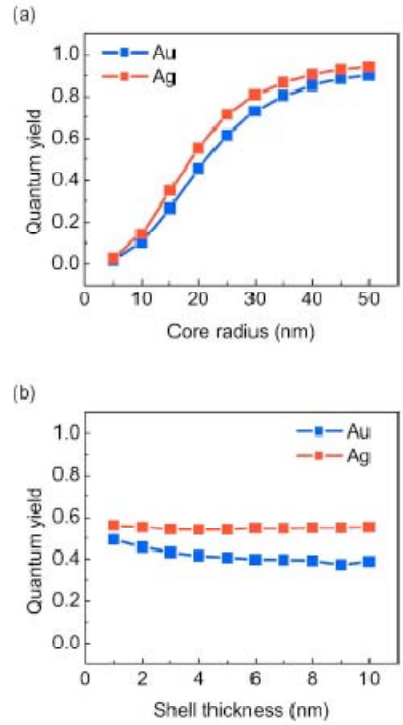

Fig. 8. (Color online) (a) Radiative quantum yield of the nanocomposite emitter versus core radius while the shell thickness is kept at 2 nm. (b) Quantum yield of the nanocomposite emitter versus shell thickness while the core radius is kept at 20 nm. In both (a) and (b), the emitter locates at the center of the particle and the emission wavelength is assumed to be 647 nm.

the quantum yield monotonically increases toward unity for both Au-shell and Ag-shell nanoparticles, when the core radius increases from 5 to 50 nm while the shell thickness is kept at 2 nm. In Fig. 8(b) we vary the shell thickness from 1 to 10 nm while the core radius is kept at 20 nm; the quantum yield barely changes for both Au-shell and Ag-shell nanoparticles. This result is surprising as intuitively a thicker Au shell absorbs more light from the emitter, which results in a lower quantum yield. However, it is important to note that the behavior of a fluorescence emitter in the core/shell nanoparticles is fundamentally different from a light source transmitting light through an Au film [31]. In the nanoscale system, the metal shell not only converts the optical energy into heat through the coupling of surface plasmons, but also modifies the spontaneous emission rate of the emitter through the Purcell effect [6]. As the metal thickness increases, the mode confinement is stronger resulting in larger Purcell effect which offsets the transmission loss.

The comparison between Figs. 8(a) and 8(b) suggests that the main factor which influences the quantum yield is the distance from the emitter to the metal surface instead of the metal shell thickness. This conclusion is further supported by the result shown in Fig. 9, where the quantum yield decreases as the emitter approaches the inner metal surface. In [23], Jin and Gao showed that the quantum yield of an Au-shell encapsulated QD can be in-

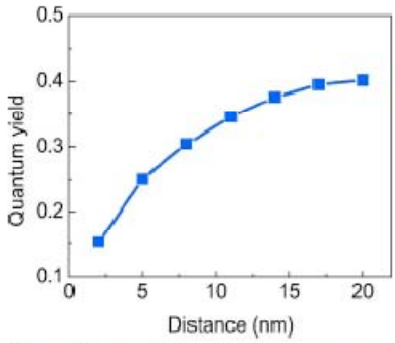

Fig. 9. (Color online) Radiative quantum yield as a function of the distance from the emitter to the inner metal surface when the core radius is 20 nm and shell thickness is 6 nm. The core and shell material are assumed to be SiO_2 and Au, respectively.

creased from 18% to 39% by coating the QD with two polyelectrolyte bilayers, which increase the core-shell separation distance from 3.1 to 4.8 nm. Such a trend is consistent with what our calculations suggest. Therefore, it is desirable to have a relatively large core radius and locate the light emitter at the center of the core, in order to minimize the non-radiative damping in the metal shell and achieve a high radiative quantum yield. Meanwhile, it is necessary to consider the upper bound of the particle size when designing the particles as biomedical imaging labels.

4. FLUORESCENCE ENHANCEMENT

Based on the studies on internal optical intensity enhancement in Section 2 and radiative quantum yield in Section 3, we discuss the fluorescence enhancement of a nanocomposite emitter in this section. We take the Alexa Fluor 633 dye as the example. The blue solid curve in Fig. 10(a) shows the absorption spectrum of the original dye with an absorption peak at 632 nm. In Section 2, we have shown that the optimized ratio between the shell thickness and core radius is approximately 0.3 for Au-shell SiO_2-core nanoparticles at this particular excitation wavelength. Here we assume that the core radius and the shell thickness of the nanoparticle are 20 and 6 nm, respectively. The absorption profile of the nanocomposite emitter can be calculated by multiplying the dye's original absorption spectrum [29] by the optical intensity enhancement [red dashed curve in Fig. 3(a)]. The obtained absorption profile of the nanocomposite emitter is shown as the red dashed curve in Fig. 10(a). Similarly, we can obtain the emission profile of the nanocomposite emitter by multiplying the dye's original emission spectrum [29] and the radiative quantum yield of the nanocomposite emitter, shown as the red dashed curve in Fig. 10(b). As can be seen, under the optimal design geometry, both the absorption and emission peaks of the dye-nanoparticle remain the same as compared to those of the original dye molecule. Because of the coupling to the core/shell nanoparticle, the emission band becomes slightly narrower, which is consistent with what researchers observed in experiment [21].

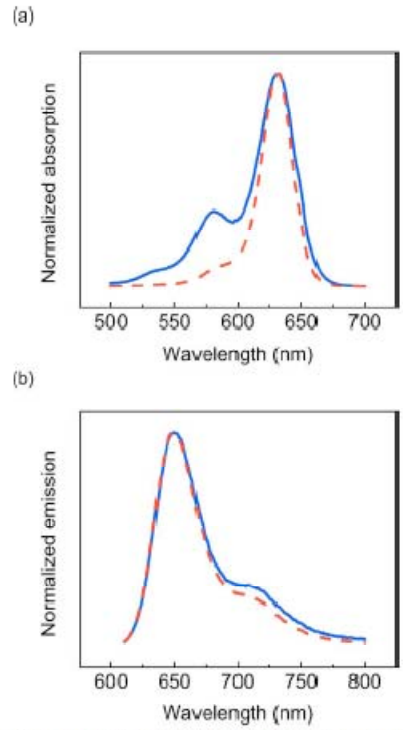

Fig. 10. (Color online) An Alexa Fluora 633 dye molecule located at the center of an Au-shell SiO_2-core nanoparticle with a 20 nm core radius and 6 nm shell thickness. (a) Absorption spectrum of the dye (blue solid curve [25]) and the nanocomposite emitter (red dashed curve). (b) Emission spectrum of the dye (blue solid curve [25]) and the nanocomposite emitter (red dashed curve).

The fluorescence enhancement of the nanocomposite emitter as compared to the dye itself can be obtained by multiplying the absorption enhancement (optical intensity enhancement) and the radiative quantum yield. The result is shown in Fig. 11 as a function of excitation and detection wavelengths. The peak enhancement is around 25, which corresponds to the excitation wavelength at 633 nm and detection wavelength at 647 nm. For the same

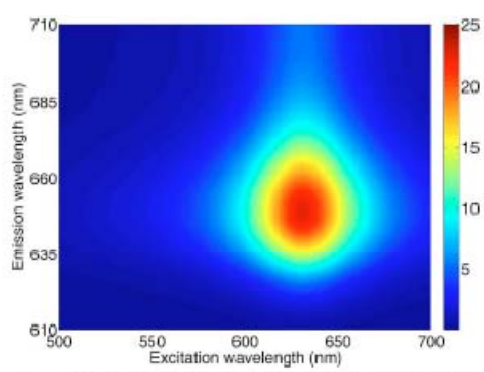

Fig. 11. (Color online) Fluorescence enhancement as a function of excitation and detection wavelength for an Alexa Fluora 633 dye molecule encapsulated at the center of an Au-shell SiO_2-core nanoparticle with a 20 nm core radius and 6 nm shell thickness.

dye molecule encapsulated in a Ag-shell SiO_2-core nanoparticle with the core radius of 50 nm and shell thickness of 8.5 nm, the peak fluorescence enhancement is around 450 (the internal optical intensity enhancement is 500 and the radiative quantum yield is 0.9). Notice that this is only the lower-bound estimate of the fluorescence enhancement since in reality the quantum yield of a fluorescence emitter is always smaller than 1.

In reality many dyes, particularly those with the emission peaks in near-infrared (NIR) have low radiative quantum yields. For instance, ICG [13] and TPQDI [10] are the two common NIR-emitting dyes, which have quantum yields of only 1.3% and 2.5%, respectively. The low intrinsic quantum yield indicates that the non-radiative decay is much stronger than the radiative decay for the dye in a homogenous background environment. When these dyes are encapsulated in core/shell nanoparticles, it is most likely that the radiative decay rates experience much higher enhancements than those of the non radiative decay rates [32]. This will result in an improvement rather than degradation of quantum yield and therefore a much higher fluorescence enhancement as compared to what has been discussed using the model of ideal dipole.

5. EXAMPLES OF CORE/SHELL NANOCOMPOSITE EMITTERS

Chemical synthesis is the main route to obtain the core/shell nanocomposite emitters in experiment. A thin metal shell is typically generated by a chemical reduction process. Specifically, an Au shell is produced by reduction of Au^{3+} in chloroauric acid solution by a reducing agent such as hydroxylamine or sodium citrate on a template particle [33,34]. Similarly, an Ag shell can be obtained by reduction of silver lactate or silver nitrate by a reducing agent such as hydroquinone [35]. The thickness of the metal shell deposited by this way ranges typically from 2 to 20 nm, which is the size range over which we performed our simulation studies. More importantly, the deposition thickness of the metal shell can be controlled by the amount of metal ions in the reaction [35].

To encapsulate an emitter inside the metal shell is the challenging part. There are a variety of approaches and here we review several representative ones. The first approach starts with linking QDs with PEG chains. The QD-PEG complex is then coated with a layer of peptide, poly-*L*-histidine, as the Au deposition template [23]. Furthermore, the core radius can be further adjusted by coating QDs with extra polyelectrolyte bilayers. Nevertheless, the technique so far only allows coating of two extra layers and this places the upper limit of the particle outer radius to around 10 nm. To simulate the optical properties of such QD-Au nanocomposite particles, it is important to take into account the finite size of QDs (the assumption of ideal dipole source and the perturbative approach to determine the field intensity in Section 2 do not hold here anymore). It is intuitive that the field intensity at the location of QD will decrease significantly due to the absorption of QD. Here we use the Au-QD nanocomposite particle in [23] as an example. The QD itself has a core/shell structure, where the core material is CdSe with a radius of about 1.5 nm and the shell material is ZnS with a thickness of about 1 nm. We consider the actual geometry of QDs in the FDTD simulation and use the bulk values of dielectric functions for CdSe and ZnS. For the core/shell nanoparticle where the QD is encapsulated, the core radius and shell thickness are 5 and 2.5 nm, respectively. The FDTD simulation result suggests that the optical intensity enhancement at the location of QD is only about 3, which is about a 50% decrease as compared to the result when there is no QD inside the nanoparticle. Furthermore, the overall small particle size results in the small separation distance between QD and metal surface, which thereby induce a strong non-radiative damping in the metal shell. The radiative quantum yield of the Au-QD nanocomposite particle is only 0.02 at the emission wavelength of the QD. Overall, the low optical intensity enhancement and low radiative quantum yield result in the quenching of fluorescence detected in far field, which is in line with the experimental results reported in [23].

The second approach is based on a reverse microemulsion process [36], where the fluorescence dye molecules are encapsulated inside the dielectric nanoparticle such as SiO_2 and TiO_2 through doping during the nanoparticle formation [19–22]. In this case, the dye molecule can exist anywhere inside the nanoparticle. When the number of dye molecules is low, we can neglect the influence of molecules to the internal electric field as the dye molecule has a much smaller size as compared to the nanoparticle. Therefore, the perturbative approach to determine the optical intensity in the nanoparticle can be used and all the dye molecules experience almost the same absorption enhancement. The radiative quantum yield of the nanoparticle encapsulated with dye molecules can therefore be averaged among all the molecules, based on the distance from the molecule to the metal surface as shown in Fig. 9. In [21], Zhang *et al.* adopted the above approach to synthesize the Ag-shell SiO_2-core nanoparticles with the $Ru(bpy)_3^{2+}$ dye molecules encapsulated inside and showed that the fluorescence emission of such nanocomposite emitters increases with the shell thickness increase from 5 to 50 nm when the core radius is fixed at 100 nm. Based on our analysis, the optimal ratio between the shell thickness and core radius to achieve maximum absorption enhancement is 0.57, which corresponds to a shell thickness of 57 nm. When the shell thickness increases from a few nanometers toward this optimal value, the optical intensity enhancement inside the nanoparticle monotonically increases and the radiative quantum yield remains almost the same. This results in the fluorescence enhancement with the shell thickness increases, as observed in experiment [21]. Interestingly, the reversed trend was observed when the dye molecules are attached at the outside of the core/shell nanoparticle [13].

The third approach is a genetically driven one based on virus assembly. A QD encapsulated virus-like particle (VLP) can be formed by attaching single QDs to hairpin ribonucleic acids that direct the formation of VLPs from multiple copies of a protein building block [37]. Such VLPs are very uniform in size and single QDs can be perfectly encapsulated at the center of a VLP [38]. Furthermore, the size of VLPs can be modified by using different

types of viruses as templates [37]. It is particularly important to note that a VLP has a relatively large size and therefore the QD encapsulated VLP can potentially possess a much higher optical intensity enhancement and radiative quantum yield.

6. CONCLUSION

In conclusion, we systematically study the optical properties of core/shell nanocomposite emitters. By encapsulating a fluorescence emitter inside the core/shell nanoparticle, localized surface plasmons of the metal shell can be harnessed to greatly enhance the fluorescence intensity of the emitter. To maximize the light absorption of the emitter, it is desirable to choose an optimized ratio between the shell thickness and core radius based on the absorption peak of the emitter. To obtain a large radiative quantum yield of the emitter-nanoparticle complex, it is required to place the emitter at a maximal distance from the inner metal surface. The optical location of the emitter is therefore at the center of a nanoparticle with as large a core radius as is pratical for a specific application.

We envision a broad range of applications based on the core/shell nanocomposite plasmonic emitters. For instance, these particles can be harnessed as ultra-bright fluorescence labels in biomedical imaging. The low degradation rate of the metal shell, particularly the Au shell, in physiological environment can enhance the biocompatibility of fluorescence labels, as well as improve the photostability of the emitters. Additionally, inspired by a recently reported plasmonic nanolaser formed by an Au core and a dye-doped silica shell [33], we intend to investigate the possibility of generating stimulated emission of surface plasmons and therefore realize lasing with the emitter inside of a dielectric-core metal-shell nanoparticle. Other than lasing, it is also promising to utilize these nanocomposite particles for assembling hybrid plasmonic waveguides [39,40] with both subwavelength confinement and long-range propagation—the metal shells mediate the energy transport and emitters provide gains to compensate for the energy loss.

ACKNOWLEDGMENTS

We thank Michael Descour, Shisheng Xiong, C. Jeffrey Brinker, Peng Zhang, and Alon Gabbay for useful discussions. This work was performed, in part, at the Center for Integrated Nanotechnologies, a U.S. Department of Energy, Office of Basic Energy Sciences user facility. The FDTD simulation portion was funded by the Energy Frontier Research Center for Solid State Lighting Science. Sandia National Laboratories is a multi-program laboratory operated by Sandia Corporation, a Lockheed-Martin Company, for the U.S. Department of Energy under Contract No. DE-AC04-94AL85000.

REFERENCES

1. S. Lal, S. Link, and N. J. Halas, "Nano-optics from sensing and waveguiding," Nature Photon. **1**, 641–648 (2007).
2. S. Kawata, Y. Inouye, and P. Verma, "Plasmonics for near-field nano-imaging and superlensing," Nature Photon. **3**, 388–394 (2009).
3. X. Miao, D. K. Wilson, S. H. Pun, and L. Y. Lin, "Optical manipulation of micron/submicron sized particles and biomolecules through plasmonics," Opt. Express **16**, 13517–13525 (2008).
4. R. A. Pala, J. White, E. Barnard, J. Liu, and M. L. Brongersma, "Design of plasmonic thin-film solar cells with broadband absorption enhancements," Adv. Mater. **21**, 3504–3509 (2009).
5. J. R. Lakowicz, K. Ray, M. Chowdhury, H. Szmacinski, Y. Fu, J. Zhang, and K. Nowaczyk, "Plasmon-controlled fluorescence: a new paradigm in fluorescence spectroscopy," Analyst (Cambridge, U.K.) **133**, 1308–1346 (2008).
6. E. M. Purcell, "Spontaneous emission probabilities at radio frequencies," Phys. Rev. **69**, 681 (1946).
7. G. Sun, J. B. Khurgin, and R. A. Soref, "Practical enhancement of photoluminescence by metal nanoparticles," Appl. Phys. Lett. **94**, 101103 (2009).
8. R. Esteban, M. Laroche, and J.-J. Greffet, "Influence of metallic nanoparticles on upconversion processes," J. Appl. Phys. **105**, 033107 (2009).
9. X. Li, J. Qian, L. Jiang, and S. He, "Fluorescence quenching of quantum dots by gold nanorods and its application in DNA detection," Appl. Phys. Lett. **94**, 063111 (2009).
10. A. Kinkhabwala, Z. Yu, S. Fan, Y. Avlasevich, K. Mullen, and W. E. Moerner, "Large single-molecule fluorescence enhancements produced by a bowtie antenna," Nature Photon. **3**, 654–657 (2009).
11. N. J. Halas, "The optical properties of nanoshells," Opt. Photonics News **13**, 26–30 (2002).
12. J. B. Jackson and N. J. Halas, "Surface-enhanced Raman scattering on tunable plasmonic substrates," Proc. Natl. Acad. Sci. U.S.A. **101**, 17930–17935 (2004).
13. R. Bardhan, N. K. Grady, and N. J. Halas, "Nanoscale control of near-infrared fluorescence enhancement using Au nanoshells," Small **4**, 1716–1722 (2008).
14. E. Dulkeith, A. C. Morteani, T. Niedereichholz, T. A. Klar, J. Friedmann, S. A. Levi, F. C. J. M. van Veggel, D. N. Reinhoudt, M. Moller, and D. I. Gittins, "Fluorescence quenching of dye molecules near gold nanoparticles: radiative and non-radiative effects," Phys. Rev. Lett. **89**, 203002 (2002).
15. P. Anger, P. Bharadwaj, and L. Novotny, "Enhancement and quenching of single-molecule fluorescence," Phys. Rev. Lett. **96**, 113002 (2006).
16. J. Enderlein, "Theoretical study of single molecule fluorescence in a metallic nanocavity," Appl. Phys. Lett. **80**, 315–317 (2002).
17. A. M. Derfus, W. C. W. Chan, and S. N. Bhatia, "Probing the cytotoxicity of semiconductor quantum dots," Nano Lett. **4**, 11–18 (2004).
18. C. J. Murphy, A. M. Gole, J. W. Stone, P. N. Sisco, A. M. Alkilany, E. C. Goldsmith, and S. C. Baxter, "Gold nanoparticles in biology: beyond toxicity to cellular imaging," Acc. Chem. Res. **41**, 1721–1730 (2008).
19. P. Zhang and Y. Cuo, "Surface-enhanced Raman scattering inside metal nanoshells," J. Am. Chem. Soc. **131**, 3808–3809 (2009).
20. W. Li, X. Miao, T. S. Luk, and P. Zhang, "Enormous average enhancement factors from SERS-tags of TiO_2-core mixed metal-shell nanoparticles," submitted to Angewandte Chemie.
21. J. Zhang, I. Gryczynski, Z. Gryczynski, and J. R. Lakowicz, "Dye-labeled silver nanoshell—bright particle," J. Phys. Chem. B **110**, 8986–8991 (2006).
22. J. Zhang, Y. Fu, and J. R. Lakowicz, "Emission behavior of fluorescently labeled silver nanoshell: enhanced self-quenching by metal nanostructure," J. Phys. Chem. C **111**, 1955–1961 (2007).
23. Y. Jin and X. Gao, "Plasmonic fluorescent quantum-dots," Nat. Nanotechnol. **4**, 571–576 (2009).
24. J. Enderlein, "Spectral properties of a fluorescing molecule within a spherical metallic nanocavity," Phys. Chem. Chem. Phys. **4**, 2780–2786 (2002).

25. U. Krebig and M. Vollmer, *Optical Properties of Metal Clusters* (Springer, 1995).
26. A. L. Aden and M. Kerker, "Scattering of electromagnetic waves from two concentric spheres," J. Appl. Phys. **22**, 1242–1246 (1951).
27. R. D. Averitt, S. L. Westcott, and N. J. Halas, "Linear optical properties of gold nanoshells," J. Opt. Soc. Am. B **16**, 1824–1832 (1999).
28. P. B. Johnson and C. Christy, "Optical constants of the noble metals," Phys. Rev. B **6**, 4370–4379 (1972).
29. http://www.invitrogen.com.
30. Y. Xu, R. K. Lee, and A. Yariv, "Quantum analysis and the classical analysis of spontaneous emission in a microcavity," Phys. Rev. A **61**, 033807 (2000).
31. S. Y. Liao, "Light transmittance and RF shielding effectiveness of a gold film on a glass substrate," IEEE Trans. Electromagn. Compat. **EMC-17**, 211–216 (1975).
32. J. B. Khurgin and G. Sun, "Enhancement of optical properties of nanoscaled objects by metal nanoparticles," J. Opt. Soc. Am. B **26**, 83–95 (2009).
33. L. R. Hirsch, A. M. Gobin, A. R. Lowery, F. Tam, R. A. Drezek, N. J. Halas, and J. L. West, "Metal nanoshells," Ann. Biomed. Eng. **34**, 15–22 (2006).
34. B. E. Brinson, J. B. Lassiter, C. S. Levin, R. Bardhan, N. Mirin, and N. J. Halas, "Nanoshells made easy: improving Au layer growth on nanoparticle surfaces," Langmuir **24**, 14166–14171 (2008).
35. J. B. Jackson and N. J. Halas, "Silver nanoshells: variations in morphologies and optical properties," J. Phys. Chem. B **105**, 2743–2746 (2001).
36. A. J. Zarur and J. Y. Ying, "Reverse microemulsion synthesis of nanostructured complex oxides for catalytic combustion," Nature **403**, 65–67 (2000).
37. M. Young, D. Willits, M. Uchida, and T. Douglas, "Plant viruses as biotemplates for materials and their use in nanotechnology," Annu. Rev. Phytopathol. **46**, 361–384 (2008).
38. X. Miao, T. S. Luk, I. Brener, C. Ashley, S. Xiong, D. Peabody, and J. Brinker, "Surface plasmon enhanced fluorescence emission inside metal nanoshells," in *Quantum Electronics and Laser Science Conference*, OSA Technical Digest CD (Optical Society of America, 2010), paper JThE20.
39. M. A. Noginov, G. Zhu, A. M. Belgrave, R. Bakker, V. M. Shalaev, E. E. Narimanov, S. Stout, E. Herz, T. Suteewong, and U. Wiesner, "Demonstration of a spaser-based nanolaser," Nature **460**, 1110–1112 (2009).
40. S. A. Maier, P. G. Kik, H. A. Water, S. Meltzer, E. Harel, B. E. Koel, and A. A. G. Requicha, "Local detection of electromagnetic energy transport below the diffraction limit in metal nanoparticle plasmon waveguide," Nature Mater. **2**, 229–232 (2003).

5. Conclusions

From the experimental studies of enhanced emission in photonic microcavities, we conclude that there is an enhancement mechanism yet to be identified. This mechanism can be non-radiative energy relaxation within the homogenous width or resonant energy transfer from the neighboring quantum dots. This is a significant effect and is worth further investigation.

Distribution

MS 1086	Dan Barton	01123
MS 1071	Andy Boye	01720
MS 1082	Igal Brener	01727
MS 1086	Weng Chow	01123
MS 1082	Michael Descour	01725
MS 1086	Art Fischer	01123
MS 1313	Sean Hearne	01132
MS 0532	James Hudgens	05340
MS 1315	Bob Hwang	08004
MS 1415	Frederick Mccormick	01110
MS 1315	Jeff Nelson	01130
MS 1080	Paul Resnick	17491
MS 1082	Ganesh Subramania	01126
MS 1421	Jerry A. Simmons	01120
MS9018	Central Technical Files	8944
MS0899	Technical library	9536 (Electronic copy)